234 (2024) 212664

Contents lists available at ScienceDirect

Geoenergy Science and Engineering

journal homepage: www.sciencedirect.com/journal/geoenergy-science-and-engineering

Characterization and reconstruction of rough fractures based on vector statistics

Mingyang Wu [a,b,c], Changbao Jiang [a,**], Bozhi Deng [a,*], Ke Gao [d], Minghui Li [e], Bo Liu [f]

[a] State Key Laboratory of Coal Mine Disaster Dynamics and Control, School of Resources and Safety Engineering, Chongqing University, Chongqing, 400030, China
[b] State Key Laboratory of Geomechanics and Geotechnical Engineering, Wuhan Institute of Rock and Soil Mechanics, Chinese Academy of Science, Wuhan, 430071, China
[c] Hubei Key Laboratory of Geo-Environmental Engineering, Institute of Rock and Soil Mechanics, Chinese Academy of Sciences, Wuhan, 430071, China
[d] Department of Earth and Space Sciences, Southern University of Science and Technology, Shenzhen, 518055, China
[e] Guangdong Provincial Key Laboratory of Deep Earth Sciences and Geothermal Energy Exploitation and Utilization, Institute of Deep Earth Sciences and Green Energy, Shenzhen University, Shenzhen, 518060, China
[f] Faculty of Earth Science and Environmental Engineering, Southwest Jiaotong University, Chengdu, 611756, China

ARTICLE INFO

Keywords:
Rough fractures
Quantitative characterization
Vector statistics
Stochastic reconstruction
Rough discrete fracture network

ABSTRACT

The characteristics of fracture networks are of great significance for unconventional geo-energy exploitation such as shale oil, shale gas and geo-thermal extraction. Natural fractures and induced fractures after reservoir stimulation control the mechanical properties and fluid flow of the reservoirs. The quantitative characterization and reconstruction of rough fractures are essential for studying the fluid flow and mechanical properties of the reservoirs with complicated fracture networks. Based on vector statistics, a vector statistical method (VSM) for quantitative characterization of rough fractures is proposed and tested using 10 standard joint profiles. Furthermore, the growth vector counting method (counting method) and growth vector probability method (probability method) for single rough fractures in two-dimensional (2D) and three-dimensional (3D) models are proposed. Afterward, a morphology comparison and quantitative evaluation of single rough fractures before and after reconstruction are conducted. When the counting and probability methods are used to reconstruct single rough fractures, the difference in the tortuosity and fractal dimensions of the original and reconstructed fractures are less than 5% and 2.5%, respectively. It implies the counting and probability methods proposed herein can reconstruct rough fractures with approximate statistical characteristics and quantitative characterization parameters. Subsequently, the counting and probability methods for single rough fractures are further developed for 2D and 3D modeling of conventional and rough discrete fracture networks. The results indicate that the growth vector counting and probability methods proposed in this study have significant potential for rough discrete fracture network modeling. In addition, the merits and limitations of the proposed algorithms in modeling discrete fracture network models are discussed.

1. Introduction

Natural fractures commonly exist in deep reservoirs, greatly affecting the development and utilization of deep fossil energy, geothermal energy, and other resources. Natural fractures usually have a certain roughness, which significantly affects the physical and mechanical properties and the development potential of deep reservoirs, such as the formation rocks properties, heat transfer capacity, reservoir flow, deformation, strength, completion, production, etc (Khang et al., 2004; Li et al., 2018; Meng et al., 2021; Pirzada et al., 2021; Sangnimnuan et al., 2018; Sun et al., 2020; Xia et al., 2021a, 2021b; Yang et al., 2020; Zhang et al., 2021). Therefore, when studying the influence of natural rough fractures on the physical and mechanical properties of rocks, a preliminary accurate knowledge of the morphology of rough fractures is necessary (Marache et al., 2002; Pan et al., 2019).

To accurately distinguish the different morphologies of rough fractures in two-dimensional (2D) and three-dimensional (3D) spaces, quantitative characterization parameters have been proposed. Owing to

* Corresponding author.
** Corresponding author.
E-mail addresses: jcb@cqu.edu.cn (C. Jiang), dengbz@cqu.edu.cn (B. Deng).

https://doi.org/10.1016/j.geoen.2024.212664
Received 29 January 2023; Received in revised form 7 November 2023; Accepted 12 January 2024
Available online 13 January 2024

the limitations of early monitoring technologies, the joint roughness coefficient (*JRC*) and path tortuosity have been proposed and widely used (Barton and Choubey, 1977; Tsang, 1984). However, the *JRC* and tortuosity focus on the overall morphology of rough fractures and disregard differences in the local characteristics of rough fractures. Subsequently, based on statistics and fractal theory (Ai et al., 2014; Li and Huang, 2015; Li and Zhang, 2015; Magsipoc et al., 2020; Marsch and Fernandez-Steeger, 2021; Wu et al., 2021a), some quantitative characterization parameters have been proposed considering the local characteristics of rough fractures. For example, the arithmetic average of the absolute height, root mean square (RMS), RMS of height, central line average, and fractal dimension measurement using different methods (e.g., compass walk method (CWM), cubic covering method (CCM), improved cubic covering method (ICCM), relative difference cubic covering method (RDCCM), and differential cubic covering method (DCCM)). Although these parameters allow single rough fractures to be conveniently quantified, the premise of quantitative evaluation of rough fractures is that the data of rough fractures have been obtained. In the current research (Jiang et al., 2019; Ju et al., 2016; Liu et al., 2016; Wu et al., 2020, 2021a, 2021b), the point cloud data of 3D or multiple rough fractures in rock specimens can be obtained using a 3D laser scanner or computed tomography (CT) scanning under static state, respectively. However, to obtain the morphological changes of fractures and fracture networks, simulation technology should be adopted. In this case, a rough fracture reconstruction based on both real and statistical data is indispensable.

Based on statistics and fractal theory, some reconstruction methods have been proposed in recent decades, for example, the Weierstrass–Mandelbrot function (Ju et al., 2017, 2019), star product fractal surfaces (Xie et al., 1999), and iterative fractal surfaces (Xie et al., 2001; Zhao, 1996). Subsequently, considering the rough and aperture characteristics of a natural fracture, many fluid flow studies were developed (Brown, 1987; Brush and Thomson, 2003; Frampton et al., 2019; Huang et al., 2019; Ogilvie et al., 2006). Based on the fractal surface generation algorithm, the fluid flow behaviour of a single rough fracture was studied (Ju et al., 2019). By combining two rough fracture surfaces, variable fracture aperture can be considered, and the fluid flow in rough-walled fractures was also simulated (Brush and Thomson, 2003; Egert et al., 2021). Unfortunately, in the simulation studies of fractured reservoirs (Feng et al., 2021; Gao et al., 2019; Lei and Gao, 2018; Lei et al., 2017, 2021; Zhu et al., 2021), the single fracture of a previous stochastic discrete fracture network (DFN) in 2D is usually treated as a straight line segment (Fig. 1b and c) (Liu et al., 2021a) and that in 3D is mostly planar (e.g., ellipse or quadrilateral) (Chen et al., 2013; Huang et al., 2021; Li et al., 2021; Smeraglia et al., 2021; Xu and Dowd, 2010). However, there are significant roughness characteristics in natural rock fractures (Fig. 1a). To distinguish different DFNs by the fracture roughness characteristics, the previous stochastic DFN ignoring the roughness of natural fractures is called C-DFN in this paper. Meanwhile, these DFN models mainly consider the distribution characteristics of the quantitative parameters (e.g., length, strike, and area) of straight and planar fractures, whereas the distribution characteristics of the quantitative parameters (tortuosity and different fractal dimensions) of the rough DFN (R-DFN) are rarely considered. Therefore, a new quantitative characterization and stochastic reconstruction method for rough fractures must be proposed. To facilitate the modeling of similar R-DFNs, a new method needs to ensure that a single rough fracture before and after reconstruction has the same statistical characteristics. Meanwhile, as we all know, image processing technology (Jing et al., 2016, 2017; Karsanina et al., 2015; Song et al., 2021a, 2021b) has been widely used in rock pore and fracture reconstruction in recent years. Therefore, to strengthen the connection with the original experiment and field data, single rough fracture features in digital images should be considered. In addition, the new method needs to be conducive to subsequent mesh generation of the R-DFN model to satisfy the requirements of large deformation and nonlinear problem simulation research.

Based on statistical theory and the connectivity characteristics of rough fractures in digital images, this paper presents a quantitative characterization and stochastic reconstruction method for single rough fractures. The principles and derivation processes are described in Section 2. Specifically, the existing characterization methods of rough fractures based on vector statistics are introduced in Section 2.1. The definition and derivation of growth vector are discussed in Section 2.2. The quantitative characterization method of rough fractures in pixel space based on vector statistics is further deduced, and the corresponding reconstruction algorithms are proposed in Section 2.3.To demonstrate its feasibility, 10 standard joint profiles in 2D are used as application tests, and the results are presented in Section 3.1. A stochastic reconstruction method of the rough fracture surface in 3D is also proposed and tested, as detailed in Section 3.2. The C-DFN and R-DFN in 2D and 3D, based on the previously proposed stochastic reconstruction algorithms, are presented in Section 4. Additionally, the merits and limitations of the proposed quantitative characterization and stochastic reconstruction methods in DFN modeling are discussed in Section 5, and the conclusions are presented in Section 6.

2. Methodologies

2.1. Quantitative characterization

The reconstruction of the R-DFN model in 2D and 3D requires a solution to the problem of quantitative characterization and stochastic reconstruction of a single rough fracture. In general, under the influence of in-situ stress, the aperture of natural fractures in reservoirs is small.

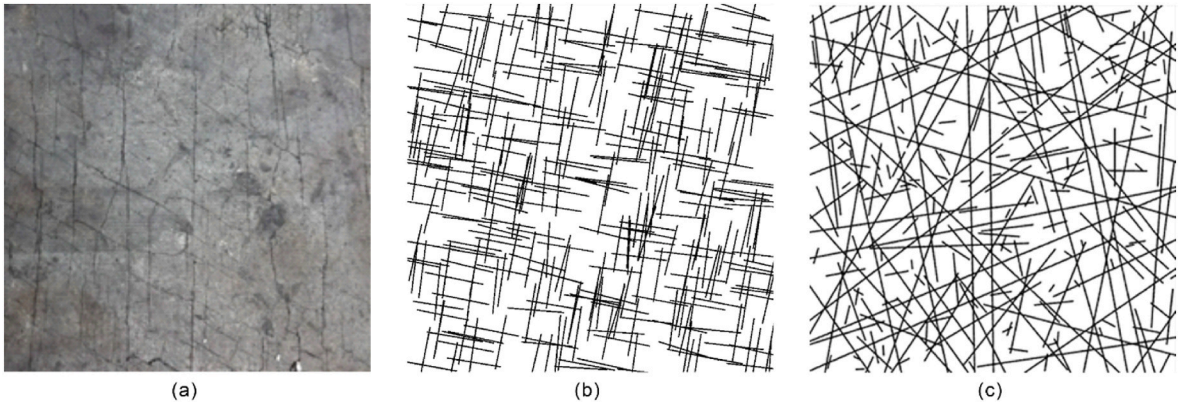

Fig. 1. Fracture networks in real rocks and simulations ((a) surface fracture network of a coal specimen, (b) fracture network in fluid simulation (Zhang et al., 2019), (c) fracture network in in-situ stress simulation).

Therefore, the natural fracture aperture relative to the fracture length is almost negligible at the reservoir scale. Meanwhile, for large deformation simulation research, to match with the current numerical simulation methods (e.g., boundary element method, block discrete element method, combined finite-discrete element method) (Ju et al., 2016; Li and Zhang, 2021; Liu et al., 2018; Wu et al., 2020, 2021b), the interface thickness (fracture aperture) is usually ignored. Under these conditions, the quantitative characterization of a single rough fracture based on vector statistics is shown in Fig. 2. As demonstrated in Fig. 2a, the rough fracture can be regarded as an irregular multi-segment line formed by the connection of many points (solid red circles). Therefore, when the connected points are established, a rough fracture is completely determined. Based on statistics (Marache et al., 2002), a rough fracture can be represented by a set of ordered points, i.e.,

$$F = \{f_i\}, f_i = (x_i, y_i, z_i), i = 1, 2, \cdots, n, \tag{1}$$

where F represents a rough fracture, and f_i is the coordinate of the ith point. The starting and ending points are $f_1 = (x_1, y_1, z_1)$ and $f_n = (x_n, y_n, z_n)$, respectively. For the entire rough fracture, a path with direction and length can be formed from starting point f_1 to ending point f_n (the longest blue arrow in Fig. 2a). The path shows the arbitrary transect direction of the entire rough fracture on the surface. To distinguish different parameters, the path is named macro growth vector, $\overrightarrow{V}_{\mathrm{F}}^{\mathrm{Macro}}$. Then, the macro growth vector, $\overrightarrow{V}_{\mathrm{F}}^{\mathrm{Macro}}$, and its length, $L_{\mathrm{F}}^{\mathrm{Macro}}$, can be expressed as

$$\overrightarrow{V}_{\mathrm{F}}^{\mathrm{Macro}} = (x_n - x_1, y_n - y_1, z_n - z_1), \tag{2}$$

$$L_{\mathrm{F}}^{\mathrm{Macro}} = \left|\overrightarrow{V}_{\mathrm{F}}^{\mathrm{Macro}}\right| = \sqrt{(x_n - x_1)^2 + (y_n - y_1)^2 + (z_n - z_1)^2}. \tag{3}$$

The rough fracture contains (n-1) line segments. Therefore, its real length, $L_{\mathrm{F}}^{\mathrm{Real}}$, can be obtained as

$$L_{\mathrm{F}}^{\mathrm{Real}} = \sum_{i=1}^{n-1} \sqrt{(x_{i+1} - x_i)^2 + (y_{i+1} - y_i)^2 + (z_{i+1} - z_i)^2}, i = 1, 2, \cdots, n-1. \tag{4}$$

Then, the fracture tortuosity (Tsang, 1984) can be expressed as $T_F = \frac{L_{\mathrm{F}}^{\mathrm{Real}}}{L_{\mathrm{F}}^{\mathrm{Macro}}}$. Meanwhile, other quantitative characterization parameters (e.g., RMS, RMS of height, JRC, and different fractal dimensions) of fracture roughness can also be obtained according to the point data of the whole fracture.

Compared with Eqs. (2)–(4), a local growth vector, $\overrightarrow{\mathbf{v}}_i$, can be used to describe the ith segment of the rough fracture:

$$\overrightarrow{\mathbf{v}}_i = (\Delta x_i, \Delta y_i, \Delta z_i) = (x_{i+1} - x_i, y_{i+1} - y_i, z_{i+1} - z_i). \tag{5}$$

Then, the real length can be calculated using the following formula by combining Eqs. (4) and (5):

$$L_{\mathrm{F}}^{\mathrm{Real}} = \sum_{i=1}^{n-1} \left|\overrightarrow{\mathbf{v}}_i\right|, i = 1, 2, \cdots, n-1. \tag{6}$$

It can be observed from Eq. (6) and Fig. 2b that a set of ordered growth vectors can be obtained:

$$V_{\mathrm{s}} = \left\{\overrightarrow{\mathbf{v}}_i\right\}, i = 1, 2, \cdots, n-1, \tag{7}$$

where V_{s} represents the set of ordered growth vectors for the rough fracture. Therefore, the rough fracture F in Fig. 2a can also be determined by the starting point f_1, and the set of ordered growth vectors V_{s}:

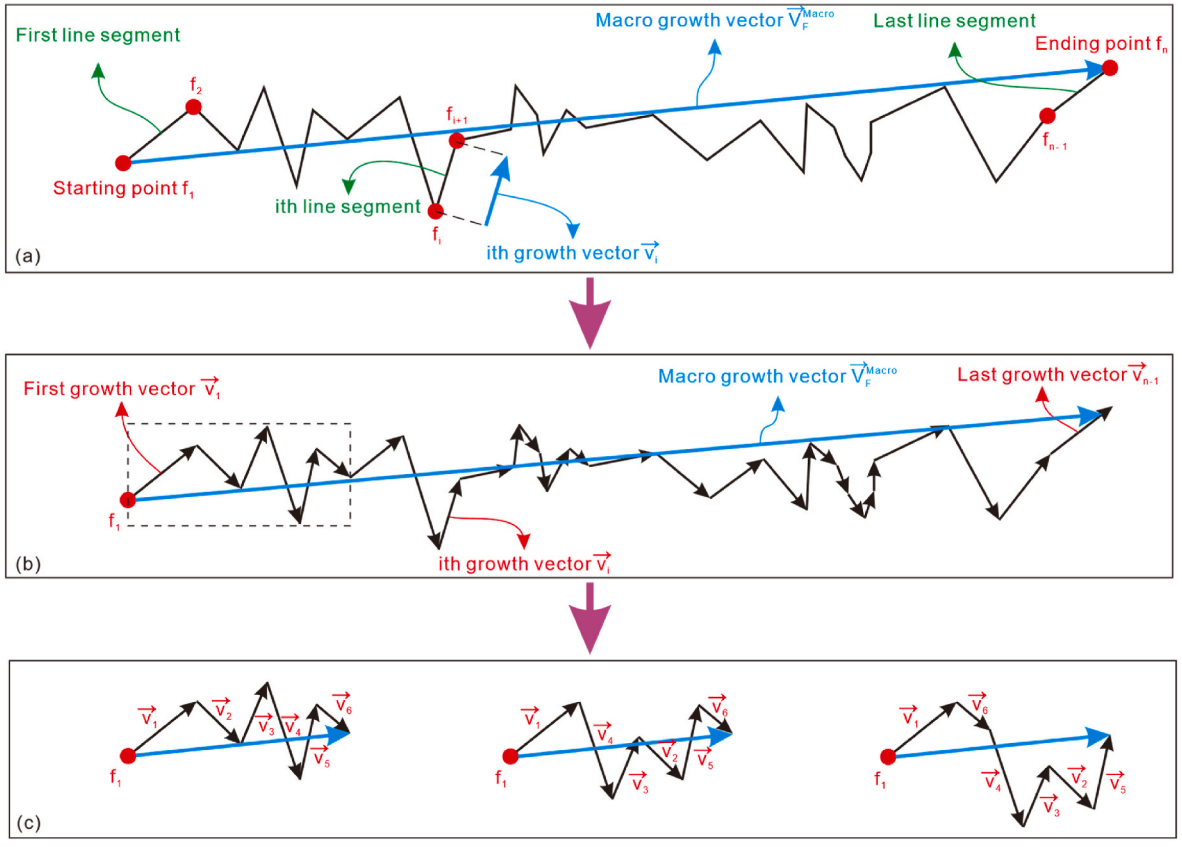

Fig. 2. Quantitative characterization sketch based on vector statistics ((a) a rough fracture in the Euclidean geometric plane, (b) vector composition diagram, and (c) different fractures obtained from the same vector set).

$$F = (f_1, V_s) = \left(f_1, \left\{\vec{\mathbf{v}}_i\right\}\right), i = 1, 2, \cdots, n-1. \tag{8}$$

It is noteworthy that the rough fracture expressed in Eq. (8) is a completely determined rough fracture. For further illustration, the rough fracture in Fig. 2a is further decomposed into vector form (Fig. 2b). After adjusting the order of the first six growth vectors of the rough fracture (Fig. 2b), different rough fractures can be formed (Fig. 2c). In Fig. 2c, the rough fracture formed by the first six ordered growth vectors $\{\vec{\mathbf{v}}_i\}, i = 1, 2, \cdots, 6$, and the starting point f_1, of the rough fracture in Fig. 2b can be expressed as $(f_1, \{\vec{\mathbf{v}}_i\}), i = 1, 2, 3, 4, 5, 6$. When the order of the growth vectors is adjusted from $\vec{\mathbf{v}}_1 \rightarrow \vec{\mathbf{v}}_2 \rightarrow \vec{\mathbf{v}}_3 \rightarrow \vec{\mathbf{v}}_4 \rightarrow \vec{\mathbf{v}}_5 \rightarrow \vec{\mathbf{v}}_6$ to $\vec{\mathbf{v}}_1 \rightarrow \vec{\mathbf{v}}_4 \rightarrow \vec{\mathbf{v}}_3 \rightarrow \vec{\mathbf{v}}_2 \rightarrow \vec{\mathbf{v}}_5 \rightarrow \vec{\mathbf{v}}_6$ or $\vec{\mathbf{v}}_1 \rightarrow \vec{\mathbf{v}}_6 \rightarrow \vec{\mathbf{v}}_4 \rightarrow \vec{\mathbf{v}}_3 \rightarrow \vec{\mathbf{v}}_2 \rightarrow \vec{\mathbf{v}}_5$, two new rough fractures can be expressed as $(f_1, \{\vec{\mathbf{v}}_i\}), i = 1, 4, 3, 2, 5, 6$ and $(f_1, \{\vec{\mathbf{v}}_i\})$, $i = 1, 6, 4, 3, 2, 5$, respectively. The starting point f_1 only affects the spatial position of the rough fracture but not the morphological characteristics (statistical proportion of different growth vectors, macro growth vector V_F^{Macro}, and real length L_F^{Real}). This indicates that if the starting point is fixed (f_1) or random (f_{random}), the statistical results of three different rough fractures in Fig. 2c are approximate; thus, they are regarded as similar rough fractures. These similar fractures F_s can then be expressed as

$$F_S = (f_{random}, V_s) = \left(f_{random}, \left\{\vec{\mathbf{v}}_i\right\}\right), i \in [1, 2, \cdots, n-1], \tag{9}$$

where $i \in [1, 2, \cdots, n-1]$ means that the growth vectors are disordered.

Eq. (9) shows that the set of growth vectors is the most important control parameter for similar rough fractures. As long as the set of growth vectors is determined, a class of similar rough fractures can be obtained. However, there may be many possible growth vectors, which render the quantitative characterization and stochastic reconstruction difficult. For example, Fig. 3a shows the result of without considering the original order of growth vectors in Fig. 2b and translating all growth vectors to the origin, before magnifying three times. Traditional characterization of rough fractures requires the identification and extraction of two pieces of information: length and angle. As shown in Fig. 3a, the fracture contains 29 different growth vectors with different directions and lengths. Due to the significant randomness of rough cracks, when extracting growth vectors, it is necessary to characterize massive random growth vectors using both length and angle information. When the number of growth vectors $n \rightarrow \infty$, the quantitative characterization and reconstruction of similar rough fractures using Eq. (9) may require a large amount of raw data and super storage capacity; this is inconvenient for practical applications. Therefore, to obtain a more practical quantitative characterization and reconstruction method, the different growth vectors in Eq. (9) must be further defined. As shown in Fig. 3b, when we standardize the length and angle of growth vectors, the information contained within the growth vectors that make up the fracture will be simplified to the selection of several standard growth vectors. This will greatly reduce the difficulty of rough crack identification and the amount of information storage, making it more suitable for digital image processing. Although, the constraints and simplification of growth vectors will affect the accuracy of fracture characterization, the impact of simplification can be disregarded, if small-scale standard growth vectors are used.

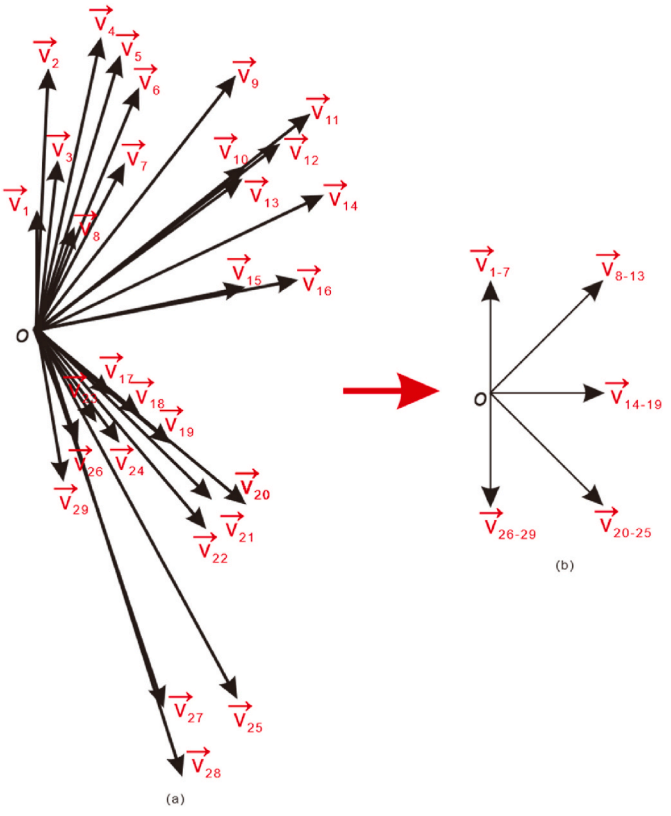

Fig. 3. Uncertainty and optimization of growth vectors. The characterization of random growth vectors using lengths and angles can be simplified as the selection of the standard growth vectors.

2.2. Definition of growth vectors

Owing to the development of monitoring technology, increased attention has been paid to obtaining rock pores and fissures from images (Wu et al., 2020, 2021b). This implies that considering the connectivity characteristics of holes and fissures in the image will be beneficial for the practical application of the new quantitative characterization and reconstruction method. Therefore, based on the connectivity feature of rough fractures in pixel space, the defining principle of growth vectors is explained. In pixel space, the connectivity of a pixel can be judged by its adjacent pixels (Bhabatosh, 1977; Gonzalez and Woods, 2002), including four neighborhoods, eight neighborhoods, and 26 neighborhoods. These finite different neighborhoods imply that the growth vectors could be defined when observing rough fractures in the pixel space. As shown in Fig. 4a and b, a rough fracture comprising multiple line segments can be regarded as being connected by a plurality of pixels in turn in the 2D pixel plane. Then, when a rough fracture is observed in the pixel space, there are only eight or 26 adjacent pixels in 2D or 3D pixel space, respectively (Fig. 4c). Therefore, the growth vectors can be further defined, and the quantitative characterization method of a rough fracture in pixel space can be further derived. Note that the pixel size may affect the fracture roughness. However, if the current image data acquisition accuracy is sufficient, and it meets the needs of numerical simulation (e.g., mesh generation, computing time), the influence of the pixel size may be reduced (Wu et al., 2021b).

Fig. 4b and c shows that there are 8 possible growth vectors of an arbitrary point of the rough fracture in 2D pixel plane; thus, the set of growth vectors V in 2D can be expressed as

$$V = \left\{\vec{v}_j\right\} = \begin{Bmatrix} -1 & -1 & & -101-1 & & 0 & 1 & 1 & 1 \\ -1 & 0 & & & & 1 & -1 & 0 & 1 \end{Bmatrix}, j = 1, 2, \cdots, 8, \tag{10}$$

where $\vec{v}_j$ represents the ith possible growth vector, and $\vec{d}_j = (V_{1j}, V_{2j}, V_{3j}), j = 1, 2, \cdots, 8$.

Fig. 4d shows different growth vectors in 3D pixel space, and a similar schematic can also be found in the lattice Boltzmann method (Ju et al., 2017). As shown in Fig. 4d, there are 26 possible growth vectors of the rough fracture in 3D pixel space; thus, the set of growth vectors V in 3D can be expressed as

$$V=\left\{\vec{v}_j\right\}=\left\{\begin{matrix}-1&-1&-1\\-1&-1&-1\\-1&0&1\end{matrix}\right.\begin{matrix}-1-1-1000-101\end{matrix}\begin{matrix}-1-1-1111-101\end{matrix}\begin{matrix}000-1-1-1-101\end{matrix}\left.\begin{matrix}0&0&0&0&0&1&1&1&1&1&1&1&1&1\\0&0&1&1&1&-1&-1&-1&0&0&0&1&1&1\\-1&1&-1&0&1&-1&0&1&-1&0&1&-1&0&1\end{matrix}\right\},\tag{11}$$

where $\vec{v}_j$ represents the ith possible growth vector, and $\vec{d}_j = (V_{1,j}, V_{2j}, V_{3j}), j = 1, 2, \cdots, 26$.

Combined with Eq. (7), the set of ordered growth vectors in Fig. 4b can be expressed as

$$V_s=\left\{\vec{\mathbf{v}}_i\right\},\ \vec{\mathbf{v}}_i\in V, i=1,2,\cdots,n-1,\tag{12}$$

where $\vec{\mathbf{v}}_i \in V$ denotes that any growth vector of the rough fracture, $\vec{\mathbf{v}}_i$, can be found in the set of different growth vectors, V, in Eq. (11). Combined with Eq. (9), similar fractures in pixel space, F_s, can be expressed as

$$F_S=\left(f_{\text{random}},\left\{\vec{\mathbf{v}}_i\right\}\right),\ \vec{\mathbf{v}}_i\in V, i\in[1,2,\cdots,n-1].\tag{13}$$

A comparison of Eqs. (9) and (13) shows that the requirement of Eq. (13) on raw data and the storage capacity have been substantially reduced after determining the set of different growth vectors. Taking a similar fracture in pixel space $F_S=\left(f_{\text{random}},\left\{\underbrace{\vec{\mathbf{v}}_1,\vec{\mathbf{v}}_5,\vec{\mathbf{v}}_{26},\cdots,\vec{\mathbf{v}}_{13},\vec{\mathbf{v}}_{16},\vec{\mathbf{v}}_{25}}_{n-1}\right\}\right)$ as an example, a rough fracture can

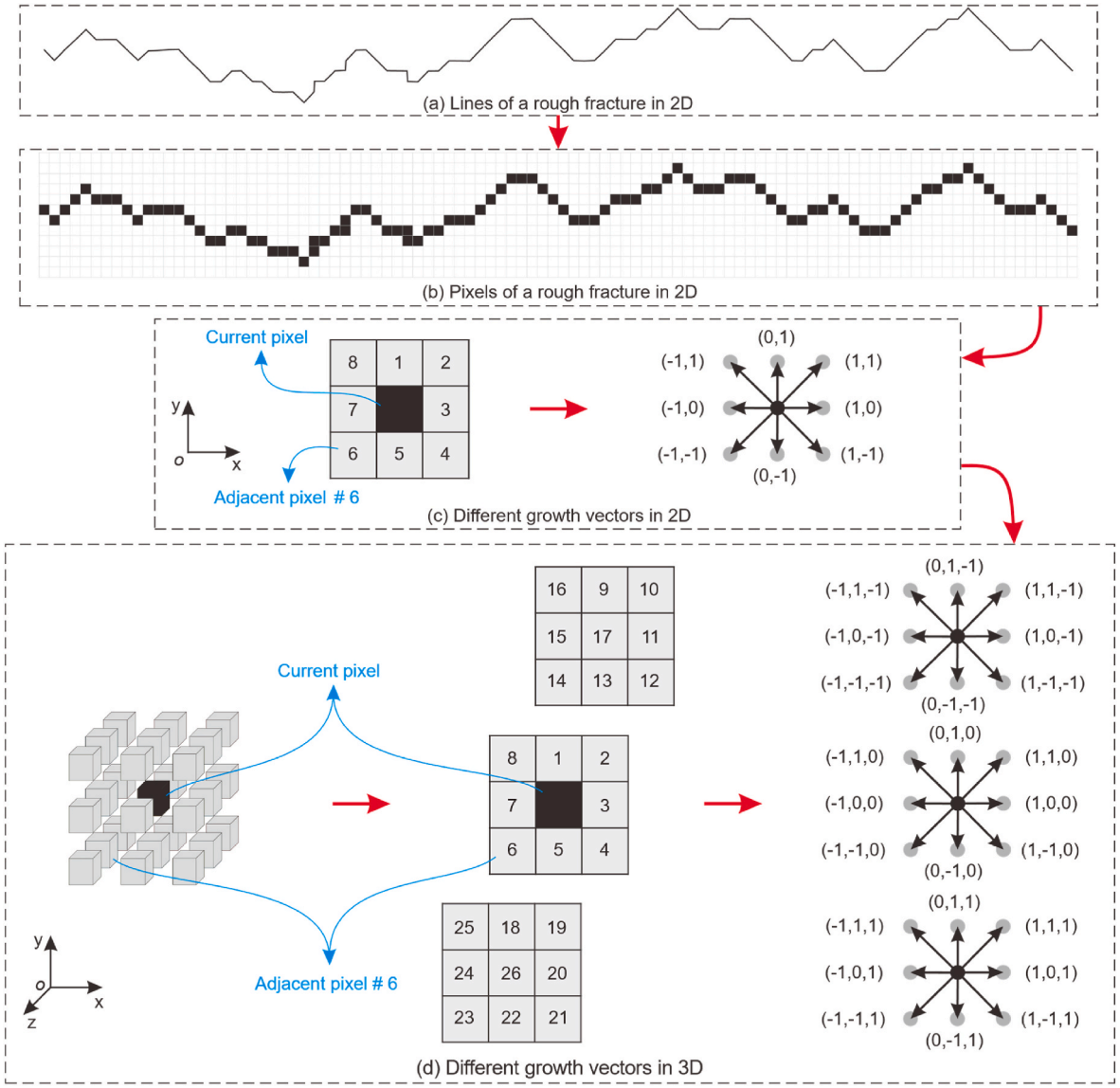

Fig. 4. Different growth vectors of a rough fracture in pixel space.

be determined when only the set of different growth vectors V and the subscript set of ordered growth vectors $\left\{\underbrace{1,5,26,\cdots,13,16,25}_{n-1}\right\}$ are known. In this case, the set of ordered growth vector subscripts of the rough fracture S can be expressed as

$$S=\{s_i\}, s_i\in[1,2,\cdots,26], i=1,2,\cdots,n-1. \tag{14}$$

Combined with Eqs. (12) and (14), the set of ordered growth vectors in pixel space F_{vs} can be expressed as

$$F_{vs}=(V,S)=(V,\{s_i\}), s_i\in[1,2,\cdots,26], i=1,2,\cdots,n-1. \tag{15}$$

Then, a completely determined rough fracture in pixel space F can be expressed by combining Eqs. (8) and (15):

$$F=(f_1,V,S)=(f_1,V,\{s_i\}), s_i\in[1,2,\cdots,26], i=1,2,\cdots,n-1, \tag{16}$$

where $i=1,2,\cdots,n-1$ indicates that the growth vectors of set S are ordered. Based on Eq. (9), similar rough fractures in pixel space can be expressed as

$$F_S=(f_{\text{random}},V,S)=(f_{\text{random}},V,\{s_i\}), s_i\in[1,2,\cdots,26], i\in[1,2,\cdots,n-1], \tag{17}$$

where $i\in[1,2,\cdots,n-1]$ implies that the growth vectors in set $S=\{s_i\}$ are disordered.

Compared with Eq. (9), Eq. (17) has made significant progress. However, the set of growth vector subscripts in Eq. (17) still requires a large amount of raw data and a super storage capacity. As the different growth vectors in pixel space are known, many repeated subscripts can be counted. Therefore, the set of the cumulative number of different growth vector subscripts C and its corresponding probability set P can be obtained:

$$C=\{c_j\}, \tag{18}$$

$$P=\{p_j\}, p_j\in[0,1], \tag{19}$$

where C is the cumulative number set of different growth vector subscripts and c_j represents the cumulative number of jth growth vectors. In 3D space, $j=1,2,\cdots,26$, $p_j=\frac{c_j}{n-1}$, and $\sum_{j=1}^{26}p_j=1$. In the 2D plane, $j=1,2,\cdots,8$, $p_j=\frac{c_j}{n-1}$, and $\sum_{j=1}^{8}p_j=1$.

In this case, similar rough fractures F_S can be expressed as

$$F_S=(f_{\text{random}},V,C) \tag{20}$$

$$F_S=(f_{\text{random}},V,P,n-1). \tag{21}$$

Obviously, different growth vectors and their corresponding cumulative numbers in any similar rough fractures, represented by Eq. (20), are always consistent. However, similar rough fractures, represented by Eq. (21), are not only controlled by the growth vector set V and cumulative probability set P, but are also affected by the number of fracture segments n-1. Therefore, to characterize similar rough fractures described in Eq. (20), the macro vector of such fractures is required for the constraint. Then, Eq. (21) can be modified as $F_S=(f_{\text{random}},V,P,n-1,V_F^{\text{Macro}})$. However, the constraint of the macro vector in fracture reconstruction may lead to many iterative calculations; this is inconvenient for practical applications. In addition, when the number of fracture segments n-1, approaches infinity, the same growth vector and statistical probability of any fracture of similar rough fractures, represented by Eqs. (20) and (21), are consistent. Therefore, Eqs. (20) and (21) are recommended as quantitative characterization formulas for similar rough fractures; this quantitative characterization method is called the vector statistical method (VSM).

2.3. Stochastic reconstruction algorithms based on vector statistical

Similar rough fractures in pixel space can be quantified using Eqs. (20) and (21). According to Eq. (20), an algorithm for obtaining similar rough fractures by the growing vector set V and its corresponding cumulative number set C can be obtained; the algorithm is referred to as the growth vector counting method (counting method). According to Eq. (21), an algorithm for obtaining similar rough fractures by the growing vector set V and its corresponding probability set P can be obtained, and

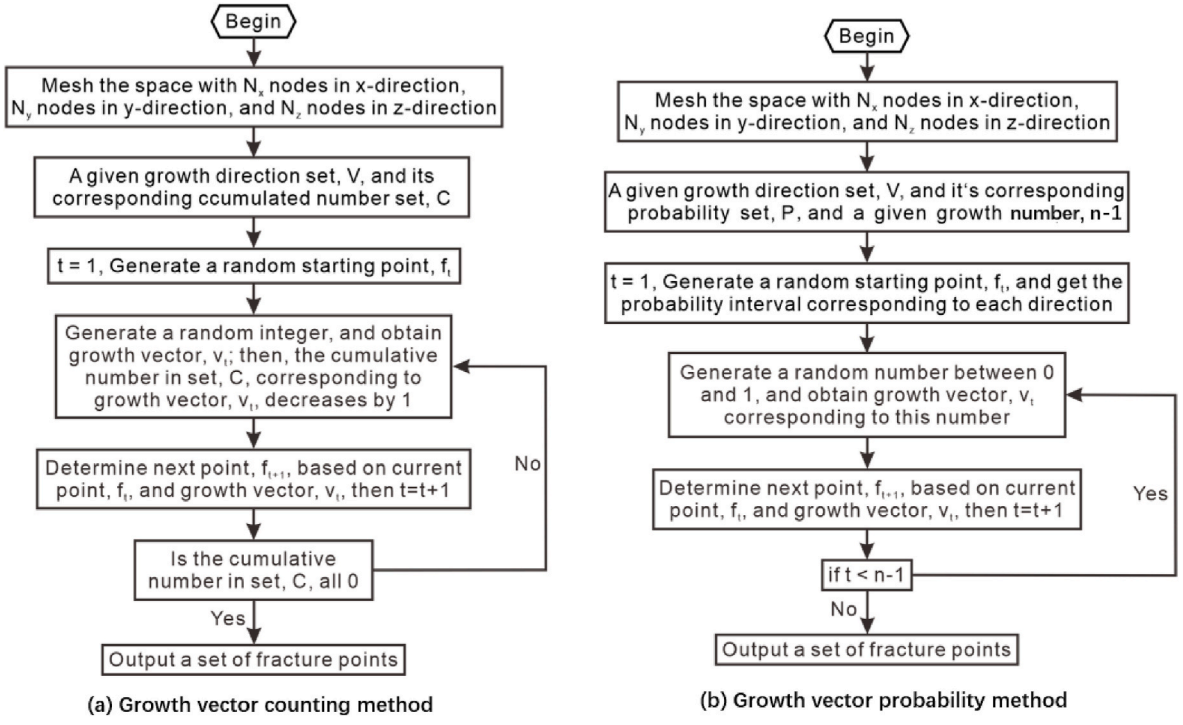

Fig. 5. Flow charts of the growth vector counting and probability methods.

the algorithm is called the growth vector probability method (probability method).

The flow charts of the counting and probability methods are shown in Fig. 5. Fig. 5a is the flow chart of the counting method, and Fig. 5b is the flow chart of the probability method. Their first step of the counting method is the same as that of the probability method, i.e., mesh the space where the rough fracture is located and set N_x, N_y, and N_z nodes in the x, y, and z directions, respectively. It should be noted that the meshed space must be larger than the space occupied by rough fractures. Then, the detailed steps of the counting method are as follows.

① Input the set of growth vectors V, and its corresponding cumulative count C.
② Assume $t = 1$ and generate a random starting point f_t.
③ A new growth vector $\vec{v}_t$ is determined based on set C. For example, assume that $V = \{(-1,-1,-1),(1,-1,0),(0,1,1)\}$ and $C = \{2,5,3\}$, thus the number of possible growth vectors (n - 1) in this example is 3. Then, a random integer between 1 and 3 is generated to determine the new growth vector $\vec{v}_t$ and the position of the next growth vector. Afterward, the cumulative count of the corresponding position in set C is subtracted by 1.
④ Determine the next fracture point f_{t+1} according to f_t and $\vec{v}_t$.
⑤ If the sum of all the cumulative numbers in the cumulative count set C is 0, the final fracture point data will be output; otherwise, continue to perform steps ③–⑤.

Meanwhile, the detailed steps of the probability method are as follows.

① Input the set of growth vectors V and its corresponding probability set P. Meanwhile, input a given growth number n-1, which is the number of cycles required to generate a present complete fracture. (i.e., the number of line segments forming the rough fracture).
② Assuming $t = 1$, a random starting point f_t can be generated and the corresponding probability interval of each growth vector can be obtained through the set of growth vectors V and its corresponding probability set P. For example, assume that $V = \{(-1,-1,-1),(1,-1,0),(0,1,1)\}$ and $P = \{0.2,0.5,0.3\}$. Then, the corresponding probability intervals of growth vectors $(-1,-1,-1)$, $(1,-1,0)$, and $(0,1,1)$ are $0-0.2$, $0.2-0.7$, and $0.7-1.0$, respectively.
③ Generate a random number between 0 and 1, and a new growth vector, $\vec{v}_t$, corresponding to the random number is determined according to the probability interval corresponding to each growth vector obtained previously. For example, if the random number is 0.1, then the new growth vector is $\vec{v}_t = (-1,-1,-1)$.
④ Determine the next fracture point, f_{t+1}, according to f_t and $\vec{v}_t$; then $t = t+1$.
⑤ If $t < n$-1, continue to perform steps ③–⑤. Otherwise, output the final fracture point data and exit the algorithm process.

3. Application tests of a single fracture

Barton and Choubey (1977) proposed the widely recognized 10 standard joint profiles by extensive shear experiments, covering rough fractures from low roughness to high roughness. Afterward, this method received widespread attention due to its ease of use and was adopted by the ISRM Committee in 1981. That is, it may be more representative and reliable than some specific experimental and simulation results. Therefore, to verify the feasibility of the VSM, counting and probability methods, 10 standard joint profiles are used for the application test. The quantitative characterization results are shown in Section 3.1.1, and the comparison results of rough fractures before and after stochastic reconstruction are presented in Section 3.1.2. Subsequently, the reconstruction algorithms for a single conventional fracture and single rough fracture surface in 3D based on the counting and probability methods are further developed and tested, as will be described in Section 3.2.

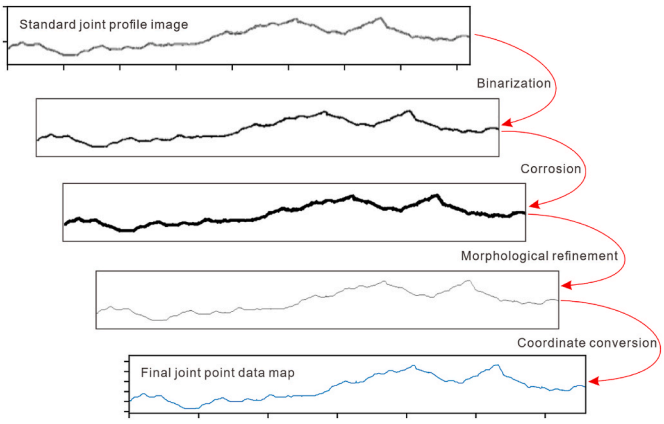

Fig. 6. Process for obtaining a set of ordered joint points.

3.1. Single rough fracture in 2D

Based on digital image processing technology, point data of 10 standard joint profiles were extracted. The detailed steps (Fig. 6) are as follows: ① To obtain more standardized raw data, the original joint profile images from Barton's research (Barton and Choubey, 1977) were first extracted. Meanwhile, to ensure measurement accuracy, joint profile images with a resolution exceeding 1600 × 300 were obtained based on digital image processing technology. ② To make the joint profile images clearer and facilitate subsequent processing, the joint profile images with sharp contrast were obtained through binarization. ③ After observation, there may be gaps in some joint profile images. To avoid the existence of gaps, the corrosion method in digital image processing is adopted to ensure the continuity of joint profiles. ④ It is generally believed that the joint profile morphology proposed by Barton (Barton and Choubey, 1977) does not consider the joint thickness, thus the refined joint profile image is obtained through morphological

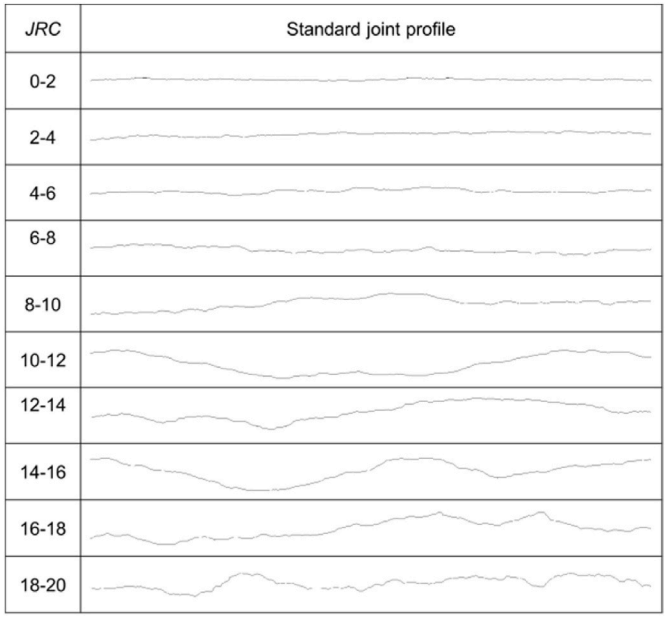

Fig. 7. Schematic diagram of the extracted 10 standard joint profile data points.

refinement processing. ⑤ The coordinates and connection data of the joint profile data points are obtained through connectivity judgment and nearest distance judgment (Wu et al., 2020, 2021b). The schematic diagram of the 10 standard joint profile data points obtained is shown in Fig. 7.

Based on the obtained coordinate point data of the 10 standard joint profiles, the quantitative characterization results obtained by the VSM are presented in Section 3.1.1. To evaluate the reliability of the counting and probability methods, the morphologies before and after reconstruction are compared. To quantitatively evaluate the reconstruction results, the fracture tortuosity (T_F) (Li and Huang, 2015) is calculated. Meanwhile, the commonly used compass walk method (CWM) (Li and Huang, 2015) and different cubic covering methods (CCM, ICCM, RDCCM, and DCCM) (Ai et al., 2014; Wu et al., 2021a) that we tested are used to quantify the differences in the rough fractures before and after reconstruction. Note that only when the fracture morphology meets the power-law distribution characteristics (Wu et al., 2021a) (i.e., the correlation coefficient of the fitting curve is close to 1), the fractal dimension can be used to characterize the rough fracture quantitatively. When different fractal dimensions of rough fractures before and after reconstruction are measured, the correlation coefficient is higher than 0.98, so different fractal dimension results can be used. The results are presented in Section 3.1.2.

3.1.1. Characterization results

According to Eq. (20), the growth vectors of the 10 standard joint profiles and their corresponding counting results are listed in Table 1. According to Eq. (21), the growth vectors of the 10 standard joint profiles and their corresponding probabilities are listed in Table 2.

Table 1 and Table 2 demonstrate that the 10 standard joint profiles with different *JRC*s are successfully quantified by eight different growth vectors in 2D, indicating that the VSM can be used for quantitatively characterizing rough fractures. For example, in Table 1, the standard joint profile with $JRC = 0-2$ can be expressed as $F_{S,JRC=0-2} = (f_{\text{random}}, V, C)$, $V = \{(0,1),(1,1),(1,0),(1,-1),(0,-1)\}$, and $C = \{1,101,1388,101,1\}$. In Table 2, the standard joint profile with $JRC = 0-2$ can be expressed as $F_{S,JRC=0-2} = (f_{\text{random}}, V, P, n-1)$, $V = \{(0,1),(1,1),(1,0),(1,-1),(0,-1)\}$, $P = \{0.0006, 0.0634, 0.8719, 0.0634, 0.0006\}$, and $n-1 = 1592$. Although there are many quantitative parameters, compared with the range value of the *JRC*, the VSM has a stronger certainty. In addition, Table 1 and Table 2 show that the 10 standard joint profiles are mainly composed of six different growth vectors ($v_1 = (0,1)$, $v_2 = (1,1)$, $v_3 = (1,0)$, $v_4 = (1,-1)$, $v_5 = (0,-1)$, and $v_6 = (-1,-1)$). Moreover, growth vector v_3 has the largest proportion, followed by growth vectors v_2 and v_4, and growth vectors v_1, v_5, and v_6 have the smallest proportion. The results indicate that these standard joint profiles have an obvious tendency, which can also be observed from the 10 standard joint profile images.

Based on the quantitative characterization results obtained by the VSM, the relationship between the peak shear strength and the *JRC* proposed by Barton (Barton and Choubey, 1977) can be briefly analyzed. The relationship between the peak shear strength and the *JRC* is

$$\tau = \sigma_n \tan\left(JRC \log\frac{JCS}{\sigma_n} + \varphi_r\right), \tag{22}$$

where τ is the peak shear strength of rock joints, σ_n is the normal stress, *JRC* is the joint roughness coefficient corresponding to the 10 standard joint profiles, *JCS* is the strength of the joint wall, and φ_r is the basic friction angle.

Eq. (22) shows that when the normal stress σ_n, strength of the joint wall *JCS*, and the basic friction angle φ_r are determined, the peak shear strength τ is positively correlated with the *JRC*. Fig. 8 shows the probability results of different growth vectors corresponding to the different *JRCs* values obtained from Table 2. First, the proportion of growth vectors $v_1 = (0,1)$, $v_5 = (0,-1)$, and $v_6 = (-1,-1)$ are lower than 0.016, 0.006, and 0.002, respectively, whereas the proportion of growth vectors $v_2 = (1,1)$, $v_3 = (1,0)$, and $v_4 = (1,-1)$ are larger. The results suggest that growth vectors v_1, v_5, and v_6 have little influence on the joint profile morphology and strength, whereas growth vectors v_2, v_3, and v_4 have a significant influence on the joint profile morphology and strength. Then, with the increase of *JRC*, the probability of growth vectors v_1, v_5, and v_6 exhibits no tendency. However, the probability of growth vectors v_2 and v_4 significantly increases, whereas the probability of growth vector v_3 significantly decreases. As shown in Fig. 4, with the increase in the *JRC*, the variation in the probability of v_2 and v_4 indicates increased fluctuation and reduced smoothness. During the shear test, with other conditions unchanged and an increase in the *JRC*, the friction coefficient of the joint profiles increases correspondingly, and the anti-sliding ability of the joint profiles increases. Therefore, the peak shear strength of rock joints is positively correlated with the *JRC*. These analysis results indicate that the relationship between the peak shear strength and the *JRC* can be better understood based on the VSM. Therefore, these results demonstrate the feasibility of the VSM. In addition, if the *JRC* can be further decomposed into the growth vector set and its probability set or the rough fracture in the shear experiment can be directly quantified, a more precise relationship between the peak shear strength of rock joints and these statistical characteristics may be obtained.

3.1.2. Comparison results

When the *JRC* is 0–2, 8–10, and 16–18, the morphology comparison results of the rough fractures before and after stochastic reconstruction are shown in Fig. 9. Of course, due to the random method, there will be some differences in the final fracture shape obtained by the same initial parameters (i.e., different random seeds and initial positions). When $JRC = 0-2$, the rough fractures reconstructed by the counting and probability methods are nearly identical to the original rough fracture. With the increase of *JRC*, the entire morphology of the reconstructed and original rough fractures significantly fluctuates. The original joint contour with $JRC = 8-10$ has a clear and relatively gentle peak, but this phenomenon was not observed in the reconstructed joint contour. There are multiple sharp peaks in the original joint contour with $JRC = 16-18$, while the peak features in the reconstructed joint contour are not

Table 1
Growth vectors and their corresponding counts of 10 standard joint profiles.

Growth vector (2D)	Cumulative count									
	0–2	2–4	4–6	6–8	8–10	10–12	12–14	14–16	16–18	18–20
(0,1)	1	0	1	4	0	0	2	0	0	27
(1,1)	101	141	131	163	185	149	190	221	247	278
(1,0)	1388	1404	1416	1313	1303	1329	1226	1215	1189	1122
(1,-1)	101	121	118	169	145	164	175	218	207	298
(0,-1)	1	0	1	4	0	0	0	2	9	4
(-1,-1)	0	0	0	1	0	0	0	1	3	0
(-1,0)	0	0	0	0	0	0	0	0	0	0
(-1,1)	0	0	0	0	0	0	0	0	0	0

Table 2
Growth vectors and their corresponding probabilities of 10 standard joint profiles.

Growth vector (2D)	Probability									
	0–2	2–4	4–6	6–8	8–10	10–12	12–14	14–16	16–18	18–20
(0,1)	0.0006	0	0.0006	0.0024	0	0	0.0013	0	0	0.0156
(1,1)	0.0634	0.0846	0.0789	0.0985	0.1133	0.0907	0.1193	0.1333	0.1492	0.1608
(1,0)	0.8719	0.8427	0.8494	0.7938	0.7979	0.8094	0.7697	0.7331	0.7183	0.6489
(1,-1)	0.0634	0.0726	0.0708	0.1022	0.0888	0.0999	0.1099	0.1318	0.1252	0.1724
(0,-1)	0.0006	0	0.0006	0.0024	0	0	0	0.0012	0.0054	0.0023
(-1,-1)	0	0	0	0.0006	0	0	0	0.0006	0.0018	0
(-1,0)	0	0	0	0	0	0	0	0	0	0
(-1,1)	0	0	0	0	0	0	0	0	0	0

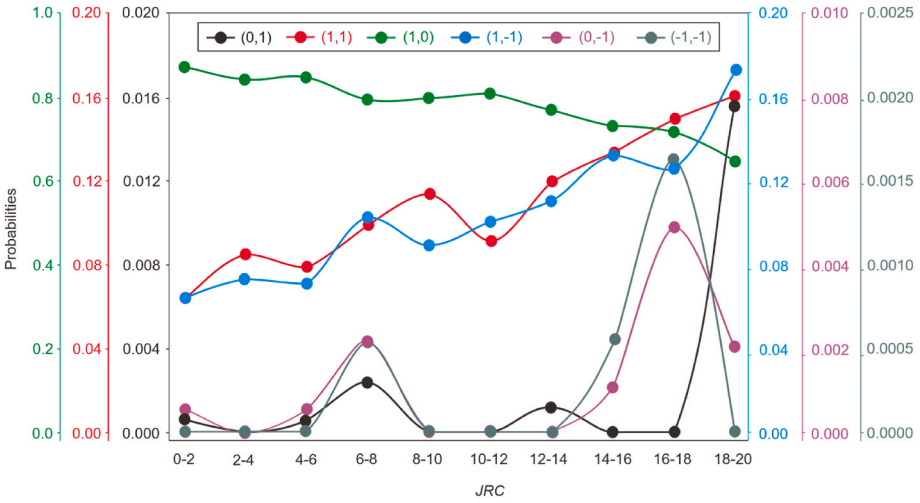

Fig. 8. Probability of different growth vectors for different *JRC*s.

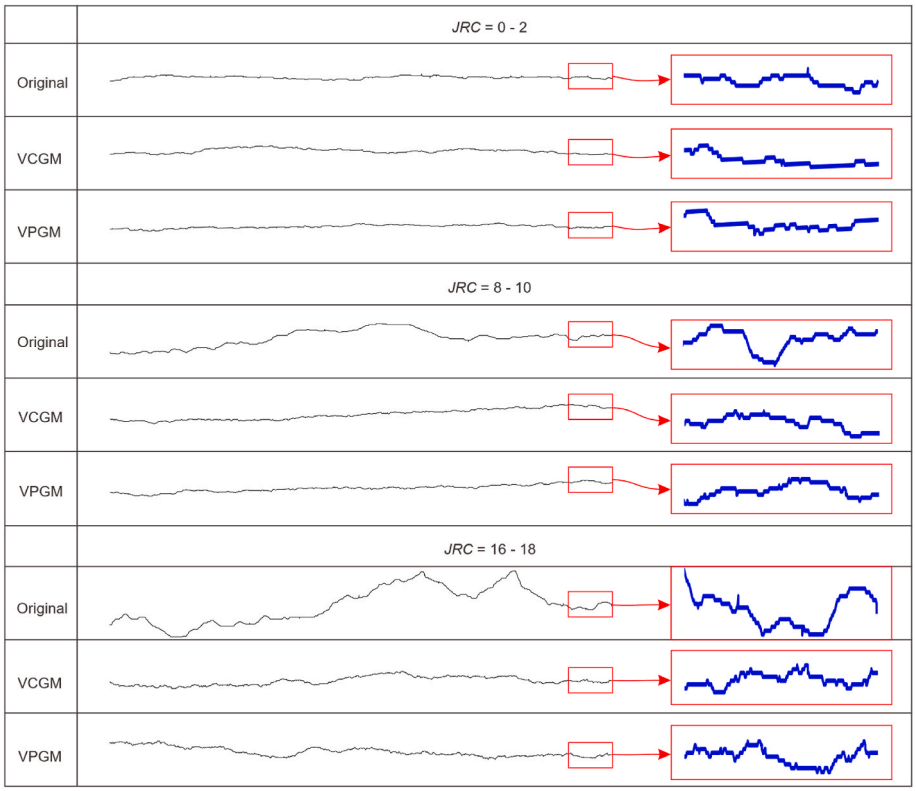

Fig. 9. Morphological comparison results of rough fractures before and after stochastic reconstruction (the original joint profiles with *JRC* of 0 – 2, 8 – 10, and 16 – 18 are from the literature (Barton and Choubey, 1977)).

significant. The results suggest that the rough fracture reconstructed by the counting and probability methods may exhibit a more obvious tendency; thus, it is more conducive to the stochastic reconstruction of tendentious rough fractures. Meanwhile, we speculate that this is due to the fact that the quantitative characterization and reconstruction methods proposed in this article only consider the overall directional probability characteristics of fractures and lack a description of the local features of fractures. In addition, the end parts of the rough fractures before and after the stochastic reconstruction are enlarged and shown in the red boxes. The morphological results (rough blue fractures) indicate that with the increase in the *JRC*, the fluctuation frequency and amplitude of the rough fractures increase significantly before and after stochastic reconstruction. This result is consistent with the definition of *JRC*, as the roughness and degree of joint contour increase with the increase of *JRC*. Therefore, these morphological comparison results indicate that the counting and probability methods proposed in this study are feasible for reconstructing similar rough fractures.

The vector statistical characteristics of rough fractures reconstructed by using the counting and probability methods are similar to those of the original fracture; hence, the statistical characteristics are not analyzed. To quantitatively evaluate whether the rough fractures reconstructed by the counting and probability methods have similar characteristics to the original rough fractures, 100 rough fractures are reconstructed. Among them, 50 rough fractures are reconstructed using the counting method, corresponding to the 10 standard joint profiles. Another 50 rough fractures are reconstructed using the probability method, corresponding to the 10 standard joint profiles. Then, the tortuosity and different fractal dimensions measured by the compass walk method (CWM), cubic covering method (CCM), improved cubic covering method (ICCM), differential cubic covering method (DCCM), and relative difference cubic covering method (RDCCM) were obtained. Subsequently, to evaluate the difference between different quantitative parameters before and after reconstruction, a difference coefficient k_{co} is calculated.

$$k_{co} = \frac{|TD_{FC} - TD_{FO}|}{TD_{FO}}, \tag{23}$$

where k_{co} is the difference coefficient, TD_{FC} and TD_{FO} represent the tortuosity or different fractal dimensions of the original and reconstructed rough fractures, respectively.

The variations in the difference coefficients of the tortuosity and different fractal dimensions before and after reconstruction are shown in Fig. 10. As can be seen, the difference coefficient of different fractal dimensions measured by the compass walk method (CWM, red), cubic covering method (CCM, green), and relative difference cubic covering method (RDCCM, orange) is less than 0.01 (1%) for the rough fractures reconstructed by using both the counting and probability methods. The difference coefficient of the tortuosity (black) and fractal dimensions measured by the improved cubic covering method (ICCM, blue) and differential cubic covering method (DCCM, purple) is less than 0.05 (5%). The results indicate that the tortuosity and different fractal dimensions before and after reconstruction are similar, demonstrating that the counting and probability methods can be used to reconstruct rough fractures with similar tortuosity and fractal dimensions. Thus, the counting and probability methods can restore not only the morphological characteristics of the original rough fractures to a certain extent, but also accurately restore similar tortuosity and fractal dimensions of the original rough fractures.

The difference coefficients of the tortuosity corresponding to different *JRCs* in Fig. 10a are almost identical; thus, they are almost concentrated in a single black data point. The result confirms that the vector statistical characteristics of rough fractures obtained by the same growth vector set are basically the same (as shown in Fig. 2). Therefore, the tortuosity of rough fractures obtained by the counting method remains the same, while there are some differences affected by probability when probability method is adopted (Fig. 10b). Meanwhile, even if the difference coefficients of the tortuosity corresponding to different *JRC*s are relatively close (the error is less than 0.05 (5%)), their results are also different (i.e., multiple black data points in Fig. 10b). To restore the reconstructed fractures with similar quantitative parameters to the original ones, they can be screened by iterative judgment. In addition, the span of the difference coefficients of fractal dimensions D_{ICCM} and D_{DCCM} in Fig. 10a is obviously smaller than that in Fig. 10b. These results indicate that the rough fracture reconstructed by the counting method has more stable tortuosity and fractal dimensions than those reconstructed by the probability method; this may be because the growth vector set and its corresponding probability set of the reconstructed rough fracture using the probability method is easily affected by the growth step. Therefore, when the growth step is small, the use of the counting method is more conducive to restoring reconstructed fractures close to the initial fracture quantitative parameters than the probability method.

3.2. Single conventional and rough fractures in 3D

Based on the VSM, counting and probability methods, different rough fracture lines in 3D can be obtained. Suppose that two 3D rough fracture lines ($F_{S,1}$, $F_{S,2}$) have been obtained. Suppose $F_{S,1}$ has n points, moving $F_{S,1}$ along $F_{S,2}$, a rough fracture surface (*RFS*) can be obtained

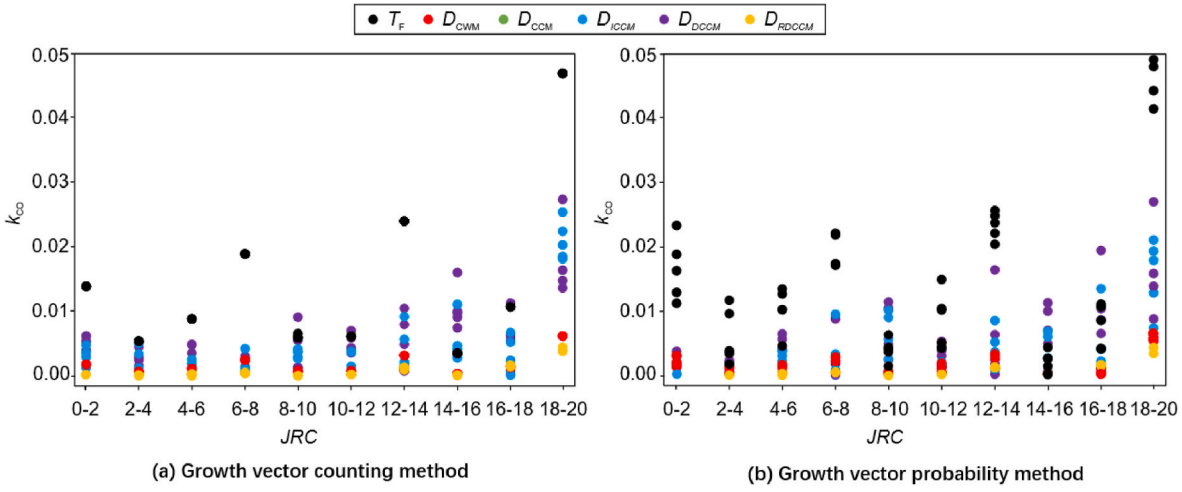

Fig. 10. Variations in difference coefficients of tortuosity and different fractal dimensions before and after reconstruction (The data of different colors represent the different results of different quantization parameters).

(Xie et al., 1999). Therefore, based on Eqs. (20) and (21), a rough fracture surface in 3D can be expressed as

$$RFS = \left(F_{S,1}, \underbrace{F_{S,2}, \cdots, F_{S,2}}_{n} \right), \tag{24}$$

where *RFS* represents a rough fracture surface constructed by two linear rough fractures ($F_{S,1}$ and $F_{S,2}$) in 3D space. It is worth noting that when a rough fracture $F_{S,1}$ is translated according to another rough fracture $F_{S,2}$ to obtain a rough fracture surface, four endpoints around the rough fracture surface can also be obtained. In this case, the four endpoints can form a finite plane, i.e., a conventional fracture surface. Therefore, not only a rough fracture surface but also a conventional fracture surface can be obtained using Eq. (24).

Generally, when testing and verifying the proposed method, there is no essential difference between real and stochastic fracture surfaces. Therefore, this section directly demonstrates the verification analysis through stochastic reconstruction results. As the main focus is on the reconstruction of a single conventional fracture or single rough fracture in 3D, random initial parameters are set and five conventional fractures and five rough fractures in 3D are constructed based on Eq. (24). As the shapes of the five reconstructed conventional fractures are identical, implying that the relative positions of the four endpoints of the conventional fractures and five rough fractures remain unchanged, the results of a conventional fracture are shown in Fig. 11a. The reconstructed five rough fractures with different shapes are shown in Fig. 11b–f. The fracture surface shown in Fig. 11a is planar and smooth, whereas the fracture surfaces presented in Fig. 11b–f are nonplanar and rough. Subsequently, different cubic covering methods are used (Ai et al., 2014; Wu et al., 2021a) to measure the 3D fracture surfaces, and the results are shown in Fig. 12. Fig. 12 shows that some fractal dimension measurement results of rough fracture surfaces are lower than 2, and that of the conventional fracture surface is not equal to 2. Similar phenomena can be observed in previous studies (Ai et al., 2014; Wu et al., 2021a), which may be caused by the rounding of the value of the measurement program. Therefore, the phenomenon is acceptable. The fractal dimensions of the five rough fractures are basically larger than those of the conventional fractures, while some of the D_{ICCM} and D_{RDCCM} of the five rough fractures are lower than those of the conventional fractures. The result

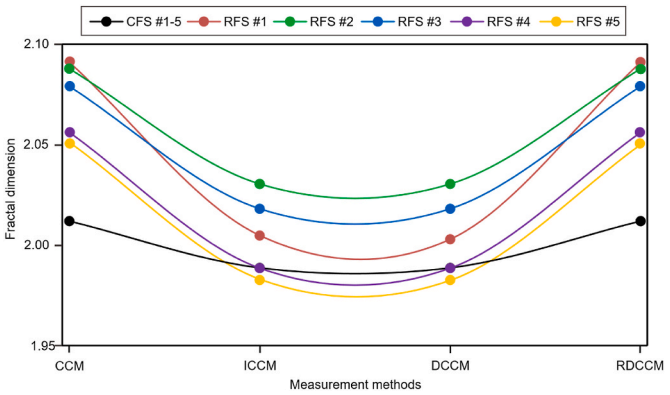

Fig. 12. Fractal dimension measurement results of conventional and rough fractures in 3D.

denotes that the improved cubic covering method (ICCM) and relative difference cubic covering method (RDCCM) need to be further improved. In addition, it can be seen from Fig. 12 that although there are differences in different fractal dimensions (D_{CCM}, D_{ICCM}, D_{DCCM}, and D_{RDCCM}) of five rough fractures, the difference coefficient is approximately 0.05 (within 2.5%). Meanwhile, the different fractal dimension results of the five reconstructed conventional fractures are consistent. Therefore, we believe that the morphological results depicted in Fig. 11 and the quantitative measurement results shown in Fig. 12 indicate that the reconstruction method of single conventional fracture and single rough fracture based on Eq. (24) is reliable. That is, it is acceptable to use the quantitative measurement results of a rough fracture to approximately reconstruct a series of similar rough fractures obtained by using Eq. (24) and the same initial parameters.

4. Application of rough fracture reconstruction in DFN models

Based on the reconstruction algorithms of single conventional and rough fractures in 2D and 3D, the reconstruction algorithms for the C-DFN and R-DFN in 2D and 3D are developed, and they are displayed in this section.

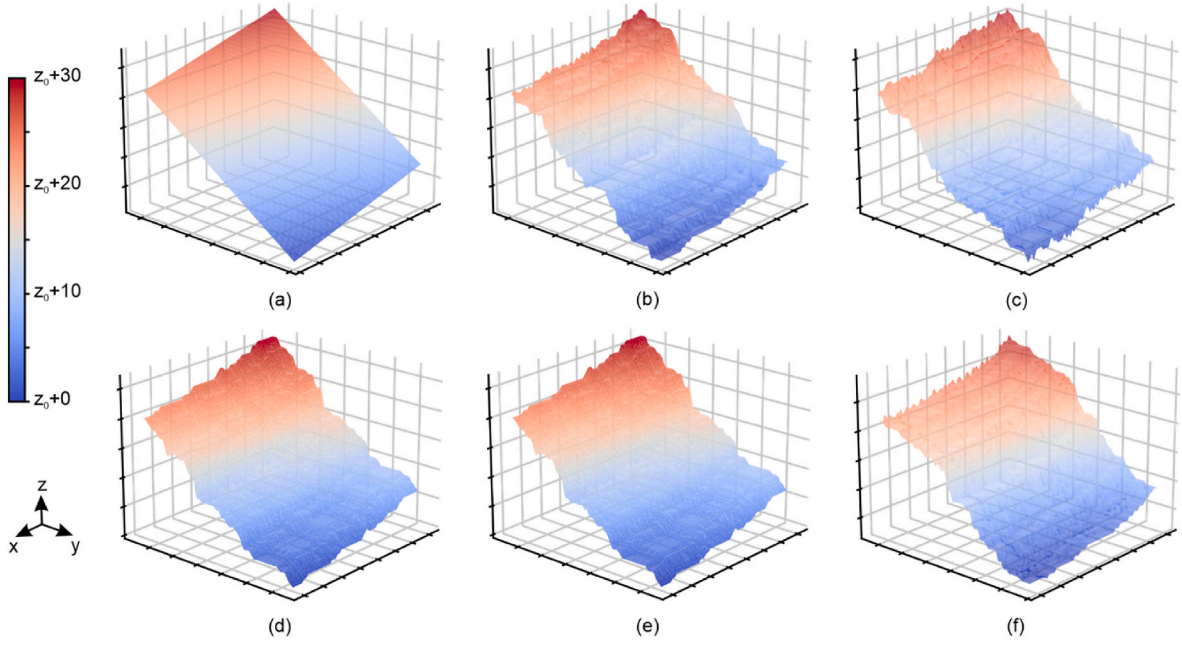

Fig. 11. Morphological results of conventional and rough fracture surfaces in 3D.

4.1. DFN models in 2D

Based on the counting and probability methods, an R-DFN in 2D can be obtained by controlling the starting point, growth vector set, corresponding count set, and probability set of single rough fractures. In this case, the R-DFN in 2D can be expressed as a set of multiple rough fractures in 2D:

$$RDFN = \{F_{S,1}, F_{S,2}, \cdots, F_{S,i}, \cdots, F_{S,m}\}, \tag{25}$$

where *RDFN* represents an R-DFN composed of *m* rough fractures in 2D. $F_{S,i}$ is the *i*th rough fracture, composed of discrete points (see Eq. (1)). When only the starting and ending points of the rough fracture are determined, a straight fracture can be obtained. When all the fractures in the network are determined, a C − DFN in 2D composed of straight fractures can also be obtained by using Eq. (25).

As the focus is on the modeling example of a C-DFN or R-DFN in 2D, the distribution characteristics of the fracture network are not considered. Therefore, the initial parameters of all fractures are set by random assignment. Subsequently, a C-DFN and a R-DFN, established using Eq. (25) are shown in Fig. 13. Note that when the start and end points of any rough fractures in the R-DFN in Fig. 13b are taken, the corresponding C-DFN in Fig. 13a can be obtained. The reconstruction results indicate that the C-DFN and R-DFN models can be obtained by using Eq. (25). Meanwhile , it is worth mentioning that Fig. 13 shows that the generated fractures have approximately three main directions: around 0°, 45°, and 135°, which is caused by the selected random initial parameters. In addition, as the 2D DFN used in the current simulations is mostly composed of multiple linear smooth fractures (Gao et al., 2019; Lei et al., 2017; Wang et al., 2021), the C-DFN and R-DFN models established in this study will help compare the differences between these two different models. In addition, as described in Sections 2.2 and 3.1, rough fractures with similar statistical characteristics, tortuosity, and fractal dimensions can be reconstructed using the counting and probability methods proposed in this paper. Therefore, the quantitative characterization and stochastic reconstruction methods proposed in this paper are also conducive to the introduction of tortuosity and different fractal dimensions into the R-DFN model in 2D.

4.2. DFN models in 3D

Based on Eq. (24), single conventional and rough fracture surfaces with close fractal dimensions can be obtained. In this case, the R-DFN in 3D can be expressed as a set of multiple rough fracture surfaces:

$$RDFN = \{RFS_1, RFS_2, \cdots, RFS_i, \cdots, RFS_m\}, \tag{26}$$

where *RDFN* represents a rough DFN in 3D composed of *m* rough fracture surfaces, and RFS_i is the *i*th rough fracture surface. In this case, if only four endpoints of any rough fracture surface in the DFN are taken, a conventional fracture surface can be formed. Subsequently, a C-DFN in 3D can also be obtained based on Eq. (26).

After random initial parameters are set, a C-DFN and a R-DFN in 3D are obtained based on Eq. (26), and the results are shown in Fig. 14. Obviously, based on the quantitative characterization and reconstruction methods proposed in this paper, both the C-DFN and R-DFN can be obtained. As confirmed in Section 3, the different fractal dimensions of a single rough fracture surface obtained by using the same initial parameters are similar. Therefore, it is helpful to introduce different fractal dimensions into the distribution model of DFNs. These results indicate that the quantitative characterization and reconstruction method proposed in this paper has considerable potential for simulation considering the influence of natural rough fracture networks.

5. Merits and limitations

DFN models have been widely used in many simulation studies such as heat and mass transfer, in situ stress evolution, and fracture propagation considering natural fracture networks (Choi et al., 2017; Deng and Zhu, 2020; Gao et al., 2019; Ju et al., 2019; Lei and Gao, 2018; Lei et al., 2017, 2021; Liu et al., 2021b). In the study of fracture simulation of large deformation rock mass, such as hydraulic fracturing of fractured rock mass, the grid quality determines the feasibility of numerical simulation and the reliability of simulation results. Therefore, this section first compares and discusses the grid quality differences of different grid models obtained by using C-DFN and R-DFN. Then, corresponding reconstruction algorithms that can be further developed are described in Section 5.2, to meet the needs of considering more random rough fractures and rough-walled fractures (Brush and Thomson, 2003; Jing et al., 2017) with the aperture in the simulation of small deformation and

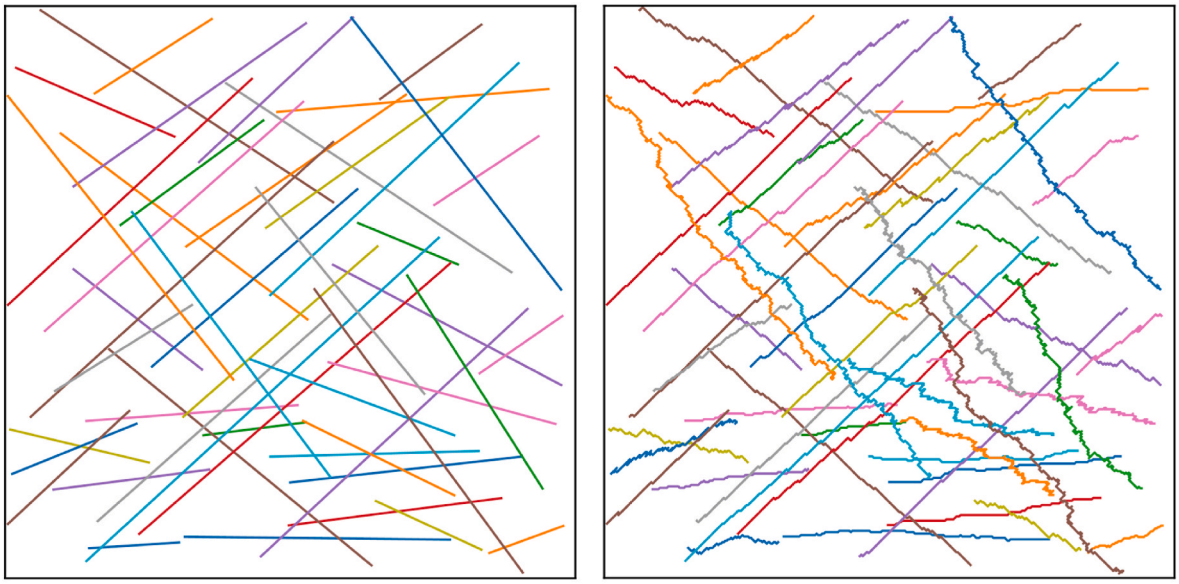

Fig. 13. Reconstruction results of the C-DFN and R-DFN in 2D.

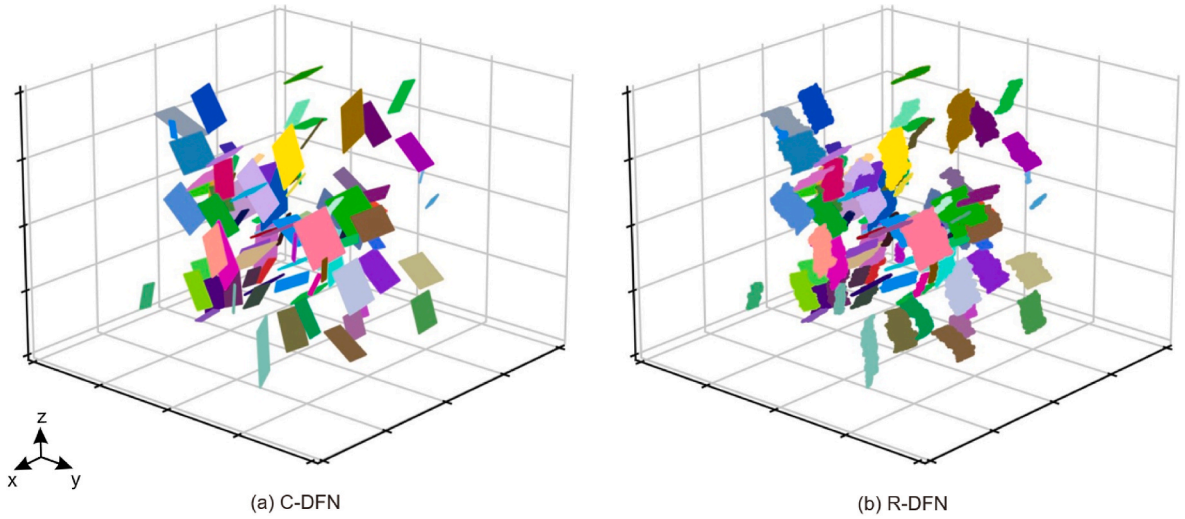

Fig. 14. Reconstruction results of the C – DFN and R – DFN in 3D.

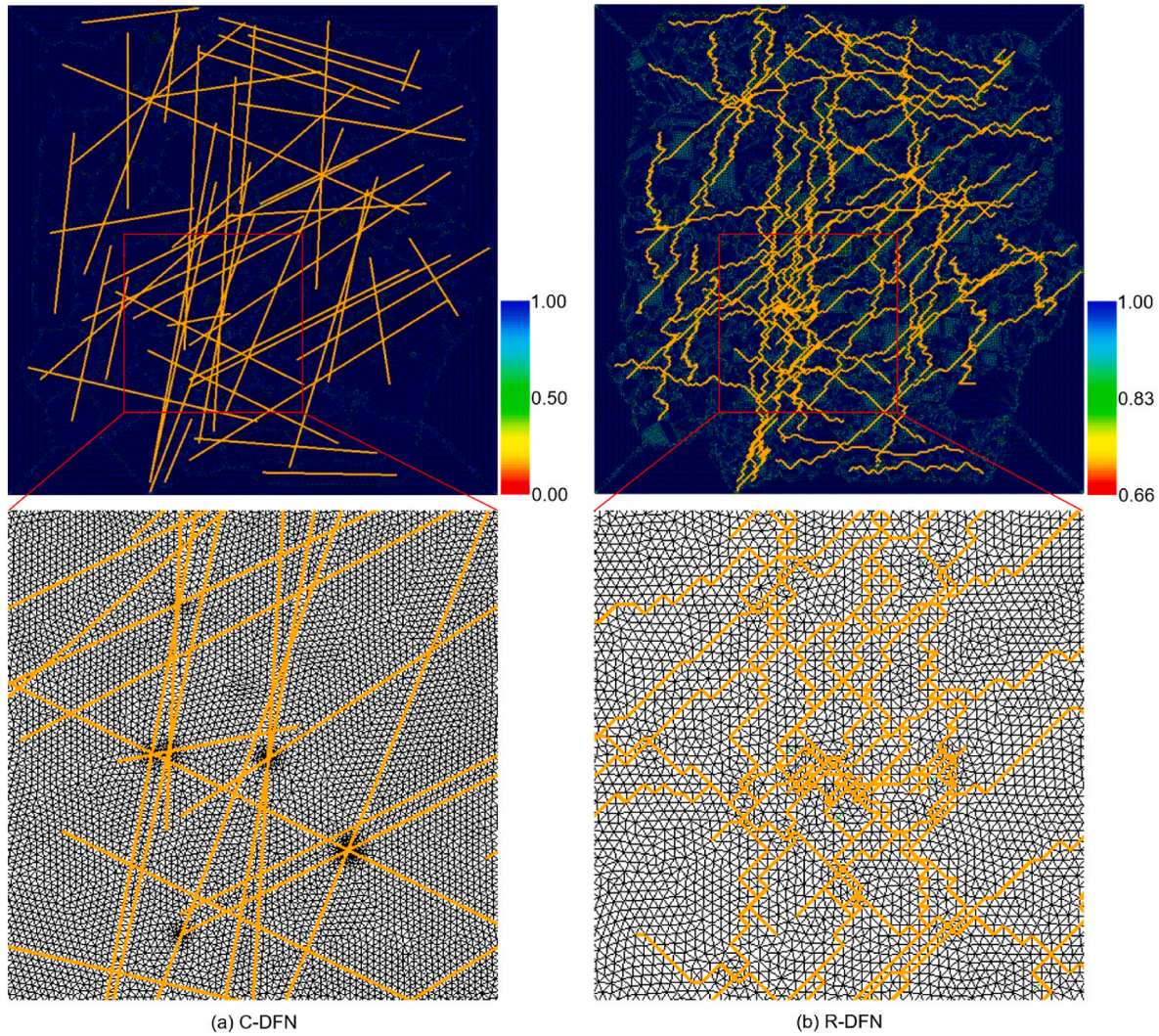

Fig. 15. Mesh generation results of the C-DFN and R-DFN models in 2D.

multi-field coupling simulation of heat and mass transfer.

5.1. Merits of mesh generation

The single fracture in C-DFN models in 2D and 3D is usually a straight line comprising two points or a planar fracture, and the proposed quantitative characterization and reconstruction method can realize the reconstruction of R-DFN models in 2D and 3D. Meanwhile, the quantitative evaluation results presented in Section 3 indicate that the tortuosity and different fractal dimensions of rough fractures obtained by using the same initial parameters do not change significantly; this will help introduce the distribution model of rough feature quantization parameters into the R-DFN models to establish a more realistic DFN model. For general small deformation problems, refining the mesh can effectively solve the convergence problem of the simulation model. Therefore, the quantitative characterization and reconstruction method of rough fractures in Section 2-4 is sufficient to support scholars in considering the influence of the R-DFN. However, large deformation and nonlinear problems, such as fracture propagation, require a higher mesh quality. Therefore, the second difficulty in applying the R-DFN models for large deformation simulations is that the established R-DFN models need to be more conducive to mesh generation to overcome the convergence problem in the simulation process.

In general, the closer the shape and size of the mesh elements in the simulation model, the better the mesh quality (Knupp, 2003). If triangular elements are used in the simulation model, closer side lengths of these elements result in a better mesh quality. In addition, the equilateral triangle element may have the best mesh quality. To evaluate the mesh quality of the R-DFN model reconstructed in this study, a C-DFN model and a R-DFN model are adopted. Then, unstructured grids of the C-DFN and R-DFN models are formed by applying the same grid generation algorithm, and the mesh quality of different models is compared based on a previous study (Knupp, 2003); the results are shown in Fig. 15. The range of the cloud image in Fig. 15 represents the shape metric of the element. A shape metric of 1 means that the triangular element is equilateral, and a shape metric of 0 means that the triangular element is degenerate. As shown in Fig. 15, the shape metric of the C-DFN model is 0–1, whereas that of the R-DFN model is 0.66–1.00. Furthermore, the local enlarged images of the C-DFN and R-DFN models show that the side lengths of the grid elements in the C-DFN model are quite different, whereas the side lengths of the grid elements in the R-DFN model are relatively similar. This may be due to the large span of the two-point connection in the C-DFN model, resulting in the formation of multiple narrow surface areas; thus, the shape and size of the triangular elements are quite different. In the R-DFN model, any rough fracture is composed of several different growth vectors; thus, it is easier to obtain triangular meshes with similar shapes and sizes in the subsequent mesh generation. These results indicate that the proposed reconstruction methods are beneficial to the mesh generation of the simulation model, providing a better solution for the simulation of large deformations and nonlinear problems (Ju et al., 2016; Li et al., 2020, 2021; Li and Zhang, 2021; Liu et al., 2018, 2021a; Wang, 2019; Wu et al., 2020). It is worth mentioning that the method proposed in this paper was written into a script program using Python language, and the different DFN models generated during the testing of this paper can be completed within a few minutes. This result indicates that using the method proposed in this paper to construct a DFN model is basically feasible in terms of time. Of course, as the proposed reconstruction method has a substantial amount of geometric information during processing, it has higher requirements for the processing ability of computer and pre-processing software.

5.2. Limitations and solutions

Under the influence of in-situ stress, the aperture of natural fractures in reservoirs is usually small. Therefore, in the study of in-situ stress and fracture propagation, 0-thick rough fracture surfaces are acceptable and widely used to match the subsequent numerical simulation methods (Wang, 2019). When small deformation heat and mass transfer simulation is carried out, the influence of fracture geometry on simulation convergence is significantly reduced. Therefore, some studies have begun to pay attention to the influence of complex random rough fractures (Brown, 1987; Jing et al., 2016, 2020). Unfortunately, the fracture surface obtained by Eq. (24) presents a certain step shape, which will not be convenient to simulate a rough fracture surface closer to the real one. When the translated rough fracture line is replaced by a series of similar rough fracture lines with statistically consistent direction vectors, a more random rough fracture surface can be obtained. Assuming that the total number of points of the first known rough fracture line is n, the number of fracture lines to be translated is n. At this time, Eq. (24) can be further improved to

$$RFS = \left(F_{S,1}, \underbrace{F_{S,2}, \cdots, F_{S,n+1}}_{n} \right), \tag{27}$$

where $F_{S,2}, \cdots, F_{S,n+1}$ represents a series of similar rough fracture lines consistent with the statistics characteristics of $F_{S,2}$.

To determine the feasibility of Eq. (27), a set of random initial parameters with greater statistical fluctuation is used to obtain rough fracture surfaces. Then, different rough fracture surfaces obtained by Eq. (24) and Eq. (27) are shown in Fig. 16a–h. Fig. 16a–h shows that the rough surfaces obtained by Eq. (24) no longer show a significant step shape (Fig. 16a, b, e, and f). Meanwhile, the elevation fluctuation of rough fractures obtained by Eq. (27) is more significant. Therefore, using Eq. (27) will be benefit to obtain a more random rough fracture surface to meet the needs of current simulation research on heat and mass transfer with small deformation. In addition, please note that the rough-walled fractures has attracted a lot of attention in a large number of fluid flow studies (Brown, 1987; Brush and Thomson, 2003; Jing et al., 2017; Ogilvie et al., 2006; Tsang, 1984; Xu and Dowd, 2010), so its random generation algorithm is also the focus of the quantitative characterization and reconstruction of rough-walled fractures. Rough-walled fractures used in previous researches (Brown, 1987; Brush and Thomson, 2003; Frampton et al., 2019; Huang et al., 2019) are usually obtained by the combination of two the same or different rough fracture surfaces. Therefore, a rough-walled fracture can be obtained by the combination of two rough fracture surfaces, as shown in Fig. 16i and j.

6. Conclusions

In this paper, a quantitative characterization method (VSM) and reconstruction methods (counting and probability methods) of single rough fractures based on vector statistics are proposed. Subsequently, standard joint profiles are used for the application test. The results show that the VSM can be used to evaluate rough fractures. With the increase in *JRC*, the proportion of growth vector $v_3 = (1,0)$ decreases, whereas the proportion of growth vectors $v_2 = (1,1)$ and $v_4 = (1,-1)$ increases. The results indicate that with the increase in *JRC*, the fracture smoothness decreases and the roughness increases. In the shear test with other conditions unchanged, the increase in the fracture surface roughness is beneficial to the improvement of the friction coefficient and anti-sliding ability. Therefore, the quantitative characterization results obtained using the VSM can explain the relationship between the *JRC* and peak shear strength, based on the statistical characteristics of rough fractures. Then, the tortuosity and different fractal dimensions measured by the compass walk method (CWM), cubic covering method (CCM), improved cubic covering method (ICCM), differential cubic covering method (DCCM), and relative difference cubic covering method (RDCCM) are used to evaluate the difference in the rough fractures in 2D before and after reconstruction. The results demonstrate that the difference

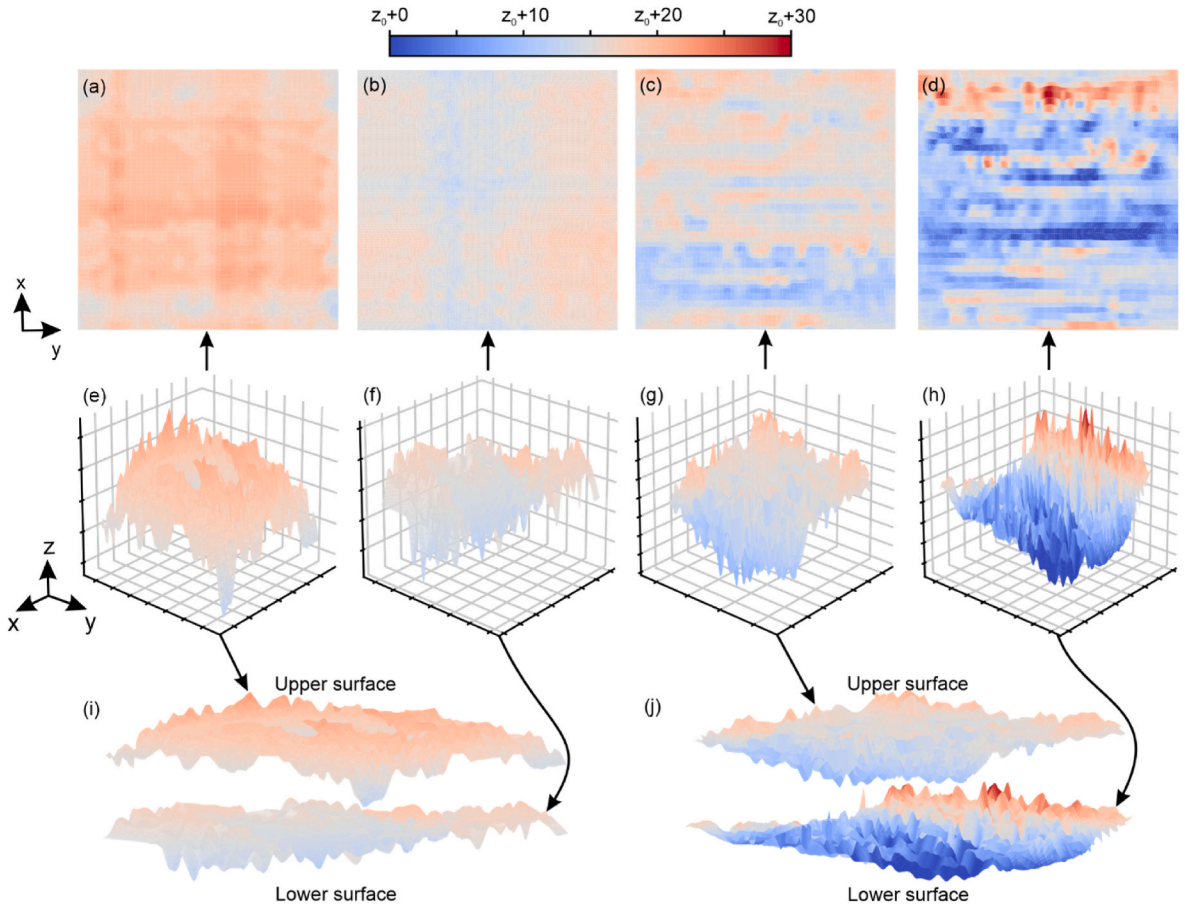

Fig. 16. Generation process of rough-walled fractures in 3D ((a), (b), (e), and (f) are two rough fracture surfaces obtained by Eq. (24) ((a) and (b) are top views, (e) and (f) are 3D views), (c), (d), (g), and (h) are two rough fracture surfaces obtained by Eq. (27) ((c) and (d) are top views, (g) and (h) are 3D views), (i) and (j) are rough walled fractures obtained by two different rough fracture surfaces, respectively).

coefficient of the tortuosity and different fractal dimensions before and after reconstruction is less than 0.05 (5%). Thus, the proposed counting and probability methods can obtain linear rough fractures with close quantitative characterization parameters. Meanwhile, the reconstruction method of single conventional and rough fractures in 3D is developed and tested, and the results show that the difference coefficient of the different fractal dimensions before and after reconstruction is less than 0.05 (within 2.5%). The results indicate that the reconstruction method of single conventional and rough fractures can obtain rough fracture surfaces with similar quantitative characterization parameters. That is, these reconstruction methods can help approximately restore the actual rough fracture morphology. Subsequently, the C-DFN and R-DFN models are established based on previous reconstruction methods, demonstrating the significant potential of the proposed quantitative characterization and reconstruction methods in DFN modeling. In addition, the mesh quality of different DFN models is discussed. The results demonstrate that the R-DFN model established in this study could help form a better quality grid. Therefore, the proposed quantitative characterization and reconstruction methods may be of great significance for establishing a fractured reservoir model that considers the rough characteristics of natural fractures.

Funding statement

The authors gratefully acknowledge the financial support given by the National Natural Science Foundation of China (42004036, 52074044 and 52204207), the National Key R&D Program of China (2022YFC3004701), Natural Science Foundation of Chongqing (CSTB2022NSCQ-MSX1593), and Special grants for postdoctoral research of Chongqing (2021XM2004).

Declaration of competing interest

The authors declare that they have no known competing financial interests or personal relationships that could have appeared to influence the work reported in this paper.

Data availability

Data will be made available on request.

Acknowledgments

We wish to thank Prof. Jianjun Liu, Chinese Academy of Science, for his guidance of this study.

References

Ai, T., Zhang, R., Zhou, H.W., Pei, J.L., 2014. Box-counting methods to directly estimate the fractal dimension of a rock surface. Appl. Surf. Sci. 314, 610–621.
Barton, N., Choubey, V., 1977. The shear strength of rock joints in theory and practice. Rock Mech. 10, 1–54.
Bhabatosh, C., 1977. Digital Image Processing and Analysis. PHI Learning Pvt. Ltd.
Brown, S.R., 1987. Fluid flow through rock joints: the effect of surface roughness. J. Geophys. Res. Solid Earth 92, 1337–1347.
Brush, D.J., Thomson, N.R., 2003. Fluid flow in synthetic rough-walled fractures: Navier-Stokes, Stokes, and local cubic law simulations. Water Resour. Res. 39.
Chen, M., Sun, Y., Fu, P., Carrigan, C.R., Lu, Z., Tong, C.H., Buscheck, T.A., 2013. Surrogate-based optimization of hydraulic fracturing in pre-existing fracture networks. Comput. Geosci. 58, 69–79.

Choi, S.B., Jeong, H.Y., Lee, S., Jeon, S., 2017. Experimental Study on Hydraulic Conductivity of a Rock Joint.
Deng, P., Zhu, J., 2020. Equivalent permeability of fractured media Incorporating tortuosity and nonlinear flow. Transport Porous Media 132, 741–760.
Egert, R., Nitschke, F., Gholami Korzani, M., Kohl, T., 2021. Stochastic 3D Navier-Stokes flow in self-affine fracture geometries controlled by anisotropy and channeling. Geophys. Res. Lett. 48, e2020GL092138.
Feng, S., Wu, Y., Liu, Y., Li, X., Wang, X., Chen, P., 2021. A fractal analysis of radon migration in discrete fracture network model. Chemosphere 266, 129010.
Frampton, A., Hyman, J.D., Zou, L., 2019. Advective transport in discrete fracture networks with connected and disconnected textures representing internal aperture variability. Water Resour. Res. 55, 5487–5501.
Gao, K., Lei, Q., Bozorgzadeh, N., Chau, V., 2019. Can we estimate far-field stress using the mean of local stresses? An examination based on numerical simulations. Comput. Geotech. 116, 103188.
Gonzalez, R.C., Woods, R.E., 2002. Digital Image Processing. Prentice hall, Upper Saddle River, NJ.
Huang, N., Jiang, Y., Liu, R., Li, B., Sugimoto, S., 2019. A novel three-dimensional discrete fracture network model for investigating the role of aperture heterogeneity on fluid flow through fractured rock masses. Int. J. Rock Mech. Min. Sci. 116, 25–37.
Huang, N., Liu, R., Jiang, Y., Cheng, Y., 2021. Development and application of three-dimensional discrete fracture network modeling approach for fluid flow in fractured rock masses. J. Nat. Gas Sci. Eng., 103957
Jiang, C., Niu, B., Yin, G., Zhang, D., Yu, T., Wang, P., 2019. CT-based 3D reconstruction of the geometry and propagation of hydraulic fracturing in shale. J. Petrol. Sci. Eng. 179, 899–911.
Jing, Y., Armstrong, R.T., Mostaghimi, P., 2017. Rough-walled discrete fracture network modelling for coal characterisation. Fuel 191, 442–453.
Jing, Y., Armstrong, R.T., Ramandi, H.L., Mostaghimi, P., 2016. Coal cleat reconstruction using micro-computed tomography imaging. Fuel 181, 286–299.
Jing, Y., Rabbani, A., Armstrong, R.T., Wang, J., Mostaghimi, P., 2020. A hybrid fracture-micropore network model for multiphysics gas flow in coal. Fuel 281, 118687.
Ju, Y., Dong, J., Gao, F., Wang, J., 2019. Evaluation of water permeability of rough fractures based on a self-affine fractal model and optimized segmentation algorithm. Adv. Water Resour. 129, 99–111.
Ju, Y., Liu, P., Chen, J., Yang, Y., Ranjith, P.G., 2016. CDEM-based analysis of the 3D initiation and propagation of hydrofracturing cracks in heterogeneous glutenites. J. Nat. Gas Sci. Eng. 35, 614–623.
Ju, Y., Zhang, Q., Zheng, J., Chang, C., Xie, H., 2017. Fractal model and lattice Boltzmann method for characterization of non-Darcy flow in rough fractures. Sci. Rep. 7, 41380.
Karsanina, M.V., Gerke, K.M., Skvortsova, E.B., Mallants, D., 2015. Universal spatial correlation functions for describing and reconstructing soil microstructure. PLoS One 10, e0126515.
Khang, N.D., Watanabe, K., Saegusa, H., 2004. Fracture step structure: geometrical characterization and effects on fluid flow and breakthrough curve. Eng. Geol. 75, 107–127.
Knupp, P.M., 2003. Algebraic mesh quality metrics for unstructured initial meshes. Finite Elem. Anal. Des. 39, 217–241.
Lei, Q., Gao, K., 2018. Correlation between fracture network properties and stress variability in geological media. Geophys. Res. Lett. 45, 3994–4006.
Lei, Q., Gholizadeh Doonechaly, N., Tsang, C.-F., 2021. Modelling fluid injection-induced fracture activation, damage growth, seismicity occurrence and connectivity change in naturally fractured rocks. Int. J. Rock Mech. Min. Sci. 138, 104598.
Lei, Q., Latham, J.-P., Tsang, C.-F., 2017. The use of discrete fracture networks for modelling coupled geomechanical and hydrological behaviour of fractured rocks. Comput. Geotech. 85, 151–176.
Li, J., Yu, W., Guerra, D., Wu, K., 2018. Modeling wettability alteration effect on well performance in Permian basin with complex fracture networks. Fuel 224, 740–751.
Li, S., Firoozabadi, A., Zhang, D., 2020. Hydromechanical modeling of nonplanar three-dimensional fracture propagation using an iteratively coupled approach. J. Geophys. Res. Solid Earth 125, e2020JB020115.
Li, S., Zhang, D., 2021. Development of 3-D curved fracture swarms in shale rock driven by rapid fluid pressure buildup: insights from numerical modeling. Geophys. Res. Lett. 48, e2021GL092638.
Li, Y., Hu, W., Zhang, Z., Zhang, Z., Shang, Y., Han, L., Wei, S., 2021. Numerical simulation of hydraulic fracturing process in a naturally fractured reservoir based on a discrete fracture network model. J. Struct. Geol., 104331
Li, Y., Huang, R., 2015. Relationship between joint roughness coefficient and fractal dimension of rock fracture surfaces. Int. J. Rock Mech. Min. Sci. 75, 15–22.
Li, Y., Zhang, Y., 2015. Quantitative estimation of joint roughness coefficient using statistical parameters. Int. J. Rock Mech. Min. Sci. 77, 27–35.
Liu, B., He, K., Han, M., Hu, X., Wu, T., Wu, M., Ma, G., 2021a. Dynamic process simulation of the Xiaogangjian rockslide occurred in shattered mountain based on 3DEC and DFN. Comput. Geotech. 134, 104122.
Liu, C., Jin, X., Shi, F., Lu, D., Liu, H., Wu, H., 2018. Numerical investigation on the critical factors in successfully creating fracture network in heterogeneous shale reservoirs. J. Nat. Gas Sci. Eng. 59, 427–439.
Liu, J., Wang, Z., Qiao, L., Li, W., Yang, J., 2021b. Transition from linear to nonlinear flow in single rough fractures: effect of fracture roughness. Hydrogeol. J. 29 (3), 1343–1353.
Liu, P., Ju, Y., Ranjith, P.G., Zheng, Z., Chen, J., 2016. Experimental investigation of the effects of heterogeneity and geostress difference on the 3D growth and distribution of hydrofracturing cracks in unconventional reservoir rocks. J. Nat. Gas Sci. Eng. 35, 541–554.
Magsipoc, E., Zhao, Q., Grasselli, G., 2020. 2D and 3D roughness characterization. Rock Mech. Rock Eng. 53, 1495–1519.
Marache, A., Riss, J., Gentier, S., Chilès, J.P., 2002. Characterization and reconstruction of a rock fracture surface by geostatistics. Int. J. Numer. Anal. Methods GeoMech. 26, 873–896.
Marsch, K., Fernandez-Steeger, T.M., 2021. Comparative evaluation of statistical and fractal approaches for JRC calculation based on a large dataset of natural rock traces. Rock Mech. Rock Eng. 54, 1897–1917.
Meng, F., Song, J., Wong, L.N.Y., Wang, Z., Zhang, C., 2021. Characterization of roughness and shear behavior of thermally treated granite fractures. Eng. Geol. 293, 106287.
Ogilvie, S.R., Isakov, E., Glover, P.W.J., 2006. Fluid flow through rough fractures in rocks. II: a new matching model for rough rock fractures. Earth Planet Sci. Lett. 241, 454–465.
Pan, D., Li, S., Xu, Z., Zhang, Y., Lin, P., Li, H., 2019. A deterministic-stochastic identification and modelling method of discrete fracture networks using laser scanning: development and case study. Eng. Geol. 262, 105310.
Pirzada, M.A., Bahaaddini, M., Moradian, O., Roshan, H., 2021. Evolution of contact area and aperture during the shearing process of natural rock fractures. Eng. Geol. 291, 106236.
Sangnimnuan, A., Li, J., Wu, K., 2018. Development of efficiently coupled fluid-flow/geomechanics model to predict stress evolution in unconventional reservoirs with complex-fracture geometry. SPE J. 23, 640–660.
Smeraglia, L., Mercuri, M., Tavani, S., Pignalosa, A., Kettermann, M., Billi, A., Carminati, E., 2021. 3D Discrete Fracture Network (DFN) models of damage zone fluid corridors within a reservoir-scale normal fault in carbonates: multiscale approach using field data and UAV imagery. Mar. Petrol. Geol. 126, 104902.
Song, R., Sun, S., Liu, J., Yang, C., 2021a. Pore scale modeling on dissociation and transportation of methane hydrate in porous sediments. Energy 237, 121630.
Song, R., Wang, Y., Sun, S., Liu, J., 2021b. Characterization and microfabrication of natural porous rocks: from micro-CT imaging and digital rock modelling to micro-3D-printed rock analogs. J. Petrol. Sci. Eng. 205, 108827.
Sun, Z., Wang, L., Zhou, J.-Q., Wang, C., 2020. A new method for determining the hydraulic aperture of rough rock fractures using the support vector regression. Eng. Geol. 271, 105618.
Tsang, Y.W., 1984. The effect of tortuosity on fluid flow through a single fracture. Water Resour. Res. 20, 1209–1215.
Wang, H., 2019. Hydraulic fracture propagation in naturally fractured reservoirs: complex fracture or fracture networks. J. Nat. Gas Sci. Eng. 68, 102911.
Wang, L., Zhou, H., Wang, J., Yu, R., Cai, J., 2021. Semi-analytical model for pumping tests in discretely fractured aquifers. J. Hydrol. 593, 125737.
Wu, M., Wang, W., Shi, D., Song, Z., Li, M., Luo, Y., 2021a. Improved box-counting methods to directly estimate the fractal dimension of a rough surface. Measurement 177, 109303.
Wu, M., Wang, W., Zhang, D., Deng, B., Liu, S., Lu, J., Luo, Y., Zhao, W., 2021b. The pixel crack reconstruction method: from fracture image to crack geological model for fracture evolution simulation. Construct. Build. Mater. 273, 121733.
Wu, M.Y., Zhang, D.M., Wang, W.S., Li, M.H., Liu, S.M., Lu, J., Gao, H., 2020. Numerical simulation of hydraulic fracturing based on two-dimensional surface fracture morphology reconstruction and combined finite-discrete element method. J. Nat. Gas Sci. Eng. 82, 103479.
Xia, B., Luo, Y., Hu, H., Wu, M., 2021a. Fractal permeability model for a complex tortuous fracture network. Phys. Fluids 33, 096605.
Xia, B., Luo, Y., Pan, C., Gong, T., Hu, H., Ji, K., 2021b. Coalbed methane flow characteristics based on fractal geometry and stochastic rough fracture network. Energy Sour, Part A Recovery, Util. Environ. Eff. 1–19.
Xie, H., Feng, S., Chen, J., 1999. On star product fractal surfaces and their dimensions. Appl. Math. Mech. 20, 1183–1189.
Xie, H., Sun, H., Ju, Y., Feng, Z., 2001. Study on generation of rock fracture surfaces by using fractal interpolation. Int. J. Solid Struct. 38, 5765–5787.
Xu, C., Dowd, P., 2010. A new computer code for discrete fracture network modelling. Comput. Geosci. 36, 292–301.
Yang, X.X., Sun, D.K., Jing, H.W., 2020. Morphological features of shear-formed fractures developed in a rock bridge. Eng. Geol. 278, 105833.
Zhang, B., Li, Y., Fantuzzi, N., Zhao, Y., Liu, Y.B., Peng, B., Chen, J., 2019. Investigation of the flow properties of CBM based on stochastic fracture network modeling. Materials 12.
Zhang, J., Li, Y., Pan, Y., Wang, X., Yan, M., Shi, X., Zhou, X., Li, H., 2021. Experiments and analysis on the influence of multiple closed cemented natural fractures on hydraulic fracture propagation in a tight sandstone reservoir. Eng. Geol. 281, 105981.
Zhao, N., 1996. Construction and application of fractal interpolation surfaces. Vis. Comput. 12, 132–146.
Zhu, W., Khirevich, S., Patzek, T.W., 2021. Impact of fracture geometry and topology on the connectivity and flow properties of stochastic fracture networks. Water Resour. Res. 57, e2020WR028652.